

Supplementary Information

Room-temperature stabilization of antiferromagnetic skyrmions in synthetic antiferromagnets

William Legrand,^{1,*} Davide Maccariello,¹ Fernando Ajejas,¹ Sophie Collin,¹ Aymeric Vecchiola,¹ Karim Bouzehouane,¹ Nicolas Reyren,¹ Vincent Cros,^{1,†} and Albert Fert¹

¹*Unité Mixte de Physique, CNRS, Thales, Univ. Paris-Sud,
Université Paris-Saclay, Palaiseau 91767, France*

* william.legrand@cnrs-thales.fr

† vincent.cros@cnrs-thales.fr

Supplementary Note 1 – Extended characterization data of multilayers

We first show how we determine both effective perpendicular anisotropy and RKKY coupling from magnetization measurements, by presenting a typical example. In Fig. S1, we display typical curves of the magnetization as a function of an applied field, in the plane and perpendicular to a multilayer [Pt(0.6 nm)/Co (1.31 nm)/Ru(0.75 nm)]₂. Both curves exhibit the standard behavior of a perpendicular SAF system. For an out-of-plane field (red curve), at field values larger than $\mu_0 H_{\text{RKKY}}$ applied in either direction, the magnetization reverses in the layer where it is opposite to the applied field and the total magnetization becomes saturated [1]. For an in-plane field (blue curve), the magnetization component in the plane of the magnetic layers $m_x = M_x/M_s$ increases linearly with the applied field before it saturates at $\pm\mu_0 H_{\text{sat}} = \mu_0 H_{\text{eff}} + 2\mu_0 H_{\text{RKKY}}$. This value of $\pm\mu_0 H_{\text{sat}}$ is because for perpendicular SAF systems, the in-plane field has to compensate for the anisotropy field $\mu_0 H_{\text{eff}} = 2K_{\text{eff}}/M_s$ and twice the RKKY coupling field $\mu_0 H_{\text{RKKY}}$ of the pair of magnetic layers, in order to bring their magnetizations into the plane [1]. As shown in Fig. S1, these saturation fields allow to extract $\mu_0 H_{\text{RKKY}}$ and $\mu_0 H_{\text{sat}} = \mu_0 H_{\text{eff}} + 2\mu_0 H_{\text{RKKY}}$. This example confirms that, as expected, [Pt/Co/Ru] multilayers can have a positive K_{eff} (strong K_u) despite the very thin Pt layer thicknesses, as well as a strong RKKY coupling that is mediated through both Ru and Pt layers. Moreover, these two measurements (in-plane and out-of-plane) are sufficient to deduce the strengths of effective anisotropy and RKKY coupling at play in our system.

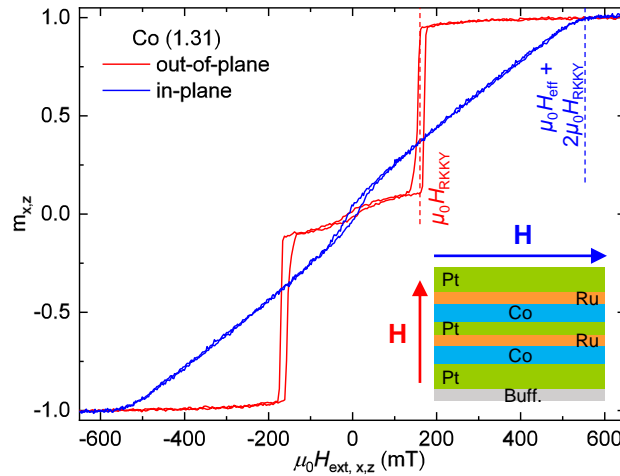


FIG. S1. Out-of-plane (red curve) and in-plane (blue curve) magnetization as a function of in-plane and out-of-plane applied field, respectively, for $t_{\text{Co}} = 1.31$ nm. They allow to extract $\mu_0 H_{\text{RKKY}}$ and $\mu_0 H_{\text{sat}} = \mu_0 H_{\text{eff}} + 2\mu_0 H_{\text{RKKY}}$, respectively (dashed lines). The scheme in inset reminds the multilayer structure, with the arrows indicating the direction of the external field applied in each case.

Additional curves of the magnetization as a function of an applied field, in the plane of the multilayer and perpendicular to the multilayer, are shown in Fig. S2, for multilayers [Pt(0.6 nm)/Co (t_{Co})/Ru(0.75 nm)]₂ with $t_{\text{Co}} = 1.15$ nm (Fig. S2a), 1.26 nm (Fig. S2b), 1.34 nm (Fig. S2c), 1.39 nm (Fig. S2d), 1.445 nm (Fig. S2e) and 1.47 nm (Fig. S2f). Consistent with the fact that both effective anisotropy and RKKY coupling decrease with t_{Co} , the in-plane saturation field $\mu_0 H_{\text{sat}}$ reduces from ≈ 850 mT to ≈ 250 mT for t_{Co} increasing from 1.15 nm to 1.47 nm. For an out-of-plane field (red curves), different behaviors occur for the magnetization perpendicular to the plane of the magnetic layers, $m_z = M_z/M_s$, in relation with the different t_{Co} values. For a strong enough perpendicular magnetic anisotropy ($t_{\text{Co}} = 1.15$ nm, 1.26 nm and 1.34 nm), the magnetization component perpendicular to the plane of the magnetic layers $m_z = M_z/M_s$ first remains very weak around zero field,

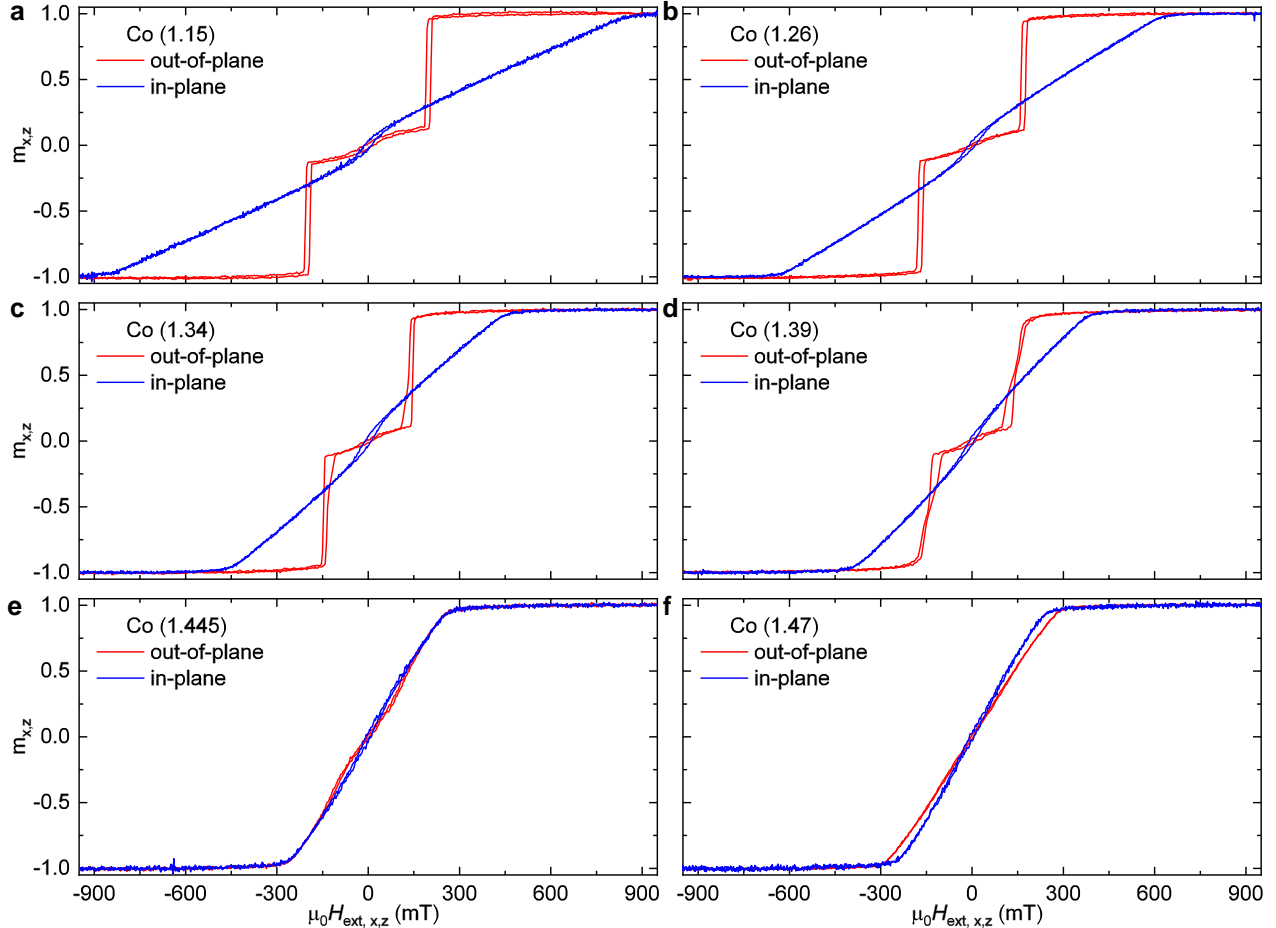


FIG. S2. Out-of-plane (red curve) and in-plane (blue curve) magnetization as a function of in-plane and out-of-plane applied field, respectively, for **a.** $t_{\text{Co}} = 1.15$ nm, **b.** $t_{\text{Co}} = 1.26$ nm, **c.** $t_{\text{Co}} = 1.34$ nm, **d.** $t_{\text{Co}} = 1.39$ nm, **e.** $t_{\text{Co}} = 1.445$ nm and **f.** $t_{\text{Co}} = 1.47$ nm.

due to a strong perpendicular anisotropy combined with RKKY coupling [1]. The magnetic configuration then corresponds to uniformly magnetized layers. Then for fields larger than $\mu_0 H_{\text{RKKY}}$ applied in either direction, as seen above, the magnetization reverses in the layer where it is opposite to the applied field and the total magnetization becomes saturated [1]. We immediately see that $\mu_0 H_{\text{RKKY}}$ is weaker in the case of $t_{\text{Co}} = 1.34$ nm (≈ 140 mT) than in the case of $t_{\text{Co}} = 1.15$ nm (≈ 200 mT), again related to its $1/t_{\text{Co}}$ dependence. In the case of $t_{\text{Co}} = 1.15$ nm, due to the stronger anisotropy, the layer reversal occurs completely at once and the curve presents sharp steps, while in the case of $t_{\text{Co}} = 1.34$ nm, the layer reversal occurs with a finite susceptibility. The curve exhibits a slope at the end of the switching that is indicative of a reversal through gradual domain expansion, due to the reduced anisotropy. For larger values of t_{Co} , above 1.35 nm, the switching is no longer a clear, open loop and $\mu_0 H_{\text{RKKY}}$ cannot be extracted anymore. In the absence of perpendicular magnetic anisotropy ($t_{\text{Co}} = 1.47$ nm), the magnetization of the layers undergo a continuous rotation from the antiferromagnetic to the ferromagnetic configuration, as for the in-plane measurement, with a linear increase followed by saturation at a field $\mu_0 H_{\text{sat}} = 2\mu_0 H_{\text{RKKY}}$ [1] for both curves. We consider the spin reorientation to be closest to $t_{\text{Co}} = 1.47$ nm, despite the small difference between the two curves, because they are both straight, opposite to the case of $t_{\text{Co}} = 1.445$ nm, and in accordance with the value extracted below.

To determine the spin reorientation transition from all previous measurements, we analyze

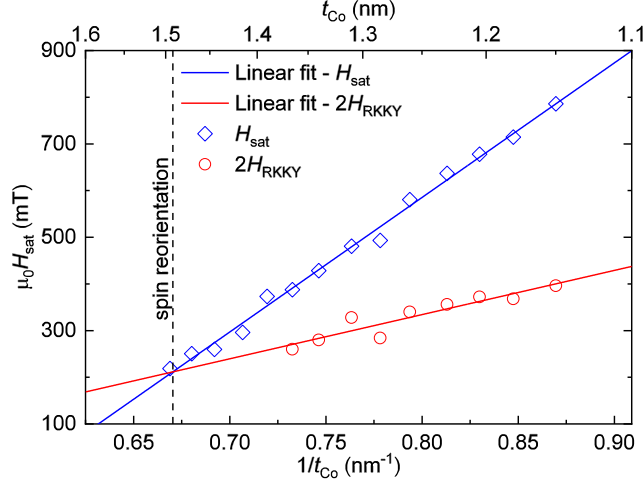


FIG. S3. Saturation field $\mu_0 H_{\text{sat}}$ (blue diamonds) and twice the RKKY coupling field $2\mu_0 H_{\text{RKKY}}$ (red circles) as a function of $1/t_{\text{Co}}$. The lines are linear fittings of the data points. The spin reorientation occurs at around $t_{\text{Co}} = 1.49$ nm (dashed vertical line).

$\mu_0 H_{\text{eff}}$ and $\mu_0 H_{\text{RKKY}}$ as a function of t_{Co} . The results are shown in Fig. S3, which displays $\mu_0 H_{\text{sat}} = \mu_0 H_{\text{eff}} + 2\mu_0 H_{\text{RKKY}}$ and $2\mu_0 H_{\text{RKKY}}$ as a function of $1/t_{\text{Co}}$. Both terms decrease with t_{Co} following the expected inverse dependence, so that $\mu_0 H_{\text{sat}}$ indeed reduces from ≈ 850 mT to ≈ 250 mT for t_{Co} increasing from 1.15 nm to 1.47 nm, while $2\mu_0 H_{\text{RKKY}}$ reduces from ≈ 400 mT to ≈ 260 mT for t_{Co} increasing from 1.15 nm to 1.365 nm. As $\mu_0 H_{\text{sat}} = \mu_0 H_{\text{eff}} + 2\mu_0 H_{\text{RKKY}}$, we can find by linear fitting of the two measurements that $K_{\text{eff}} = 0$ at around $t_{\text{Co}} = 1.49$ nm (see Fig. S3), at which thickness the system undergoes spin reorientation transition from out-of-plane to in-plane. The values of $\mu_0 H_{\text{eff}}$ as a function of $1/t_{\text{Co}}$ are deduced from the values of $\mu_0 H_{\text{sat}}$ by removing the fit corresponding to $2\mu_0 H_{\text{RKKY}}$. Note that the intercept of the fit of $\mu_0 H_{\text{eff}}$ is close to $-\mu_0 M_{\text{s}}$ (not appearing here), which indicates that the contribution of bulk anisotropy to the perpendicular magnetic anisotropy is very weak.

We now detail the conception of the bias layer (BL) and the choice of [Pt/Co]-based symmetrical multilayers to play this role, instead of more standard SAF multilayers or antiferromagnetic layers such as IrMn [2]. This choice is related to material issues, as the growth of such Pt/Co multilayers does not affect the properties of the SAF deposited above it. Also, compared to a standard SAF, a single Pt/Co multilayer allows reducing the total magnetic moment per area, to avoid transition of the whole system to ferromagnetic stripes ordering in SAF multilayers with too many layers [3]. We have tried different respective thicknesses of Pt and Co inside the multilayer. We report in Fig. S4a out-of-plane magnetization loops obtained for a series of BLs with different Co layer thicknesses, in the range 0.4–0.8 nm, for Pt layer thickness $t_{\text{Pt}} = 0.45$ nm. For too thin Co layers, such as $t_{\text{Co}} = 0.4$ nm, the BL is not able to provide a strong coercivity. For too thick Co layers, such as $t_{\text{Co}} = 0.8$ nm, the dipolar effects become more important and reduce the sharpness of the switching. We also show other out-of-plane measurements of BLs with $t_{\text{Pt}} = 0.6$ nm (Fig. S4b) and $t_{\text{Pt}} = 0.75$ nm (Fig. S4c). These curves appear similar to the ones obtained for $t_{\text{Pt}} = 0.45$ nm, however, they exhibit less sharp switching, which may indicate an increased influence of internal dipolar fields. We thus decided to use $t_{\text{Pt}} = 0.45$ nm, which should also provide more strongly coupled layers, but note that these small differences of behaviors do not appear to be critical for designing BL-SAF systems.

In Figs. S5a–c, we report the magnetization hysteresis curves of the SAF multilayers studied in the main part of the article [(i) a SAF possessing a significant effective PMA (Fig. S5a), (ii) a

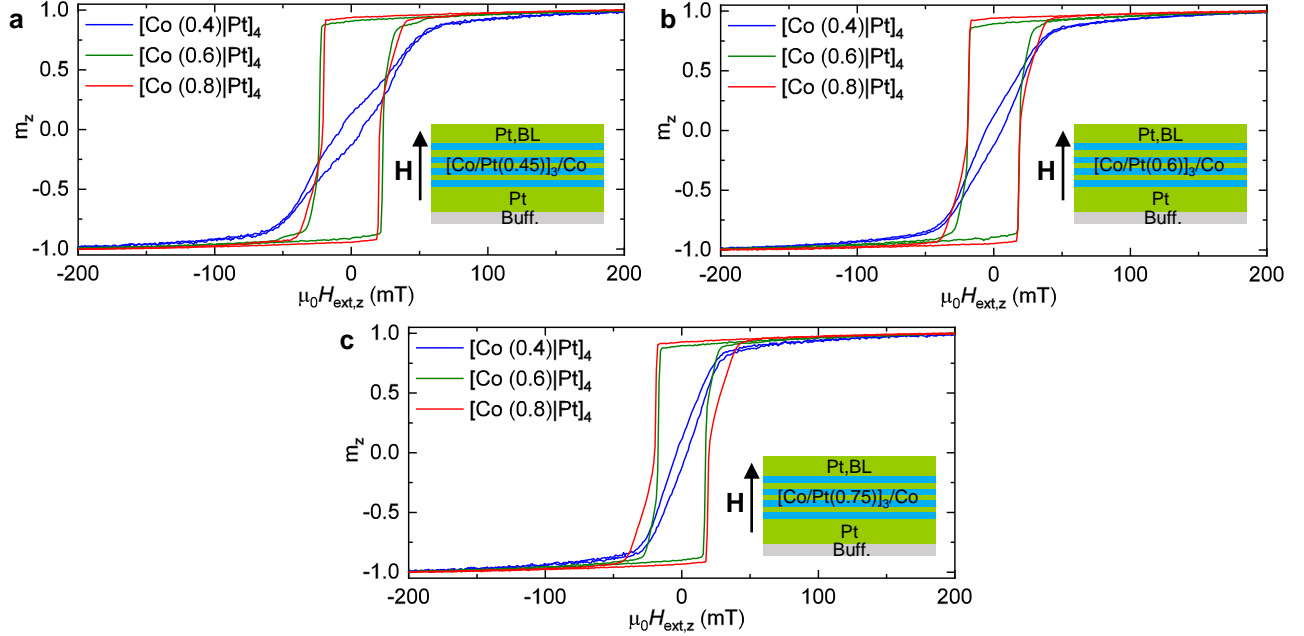


FIG. S4. Out-of-plane magnetization loops for BL with $t_{\text{Co}} = 0.4$ nm (blue), 0.6 nm (green) and 0.8 nm (red), for Pt layer thicknesses **a.** $t_{\text{Pt}} = 0.45$ nm, **b.** $t_{\text{Pt}} = 0.6$ nm and **c.** $t_{\text{Pt}} = 0.75$ nm. The scheme in inset reminds the BL structure, with the arrow indicating the direction of the externally applied field.

SAF with a vanishing effective PMA (Fig. S5b), and (iii) a SAF combining a vanishing effective PMA and a BL (Fig. S5c) as a function of an out-of-plane applied field. As expected, the SAF with effective perpendicular anisotropy displays a central plateau between two switching steps corresponding to reversal of either Co layer and the magnetization of the SAF with vanishing effective perpendicular anisotropy undergoes a continuous rotation from the antiferromagnetic to the ferromagnetic configuration. For the BL-SAF, the continuous rotation from the antiferromagnetic to the ferromagnetic configuration in the SAF is combined with the open perpendicular switching loop of the BL underneath.

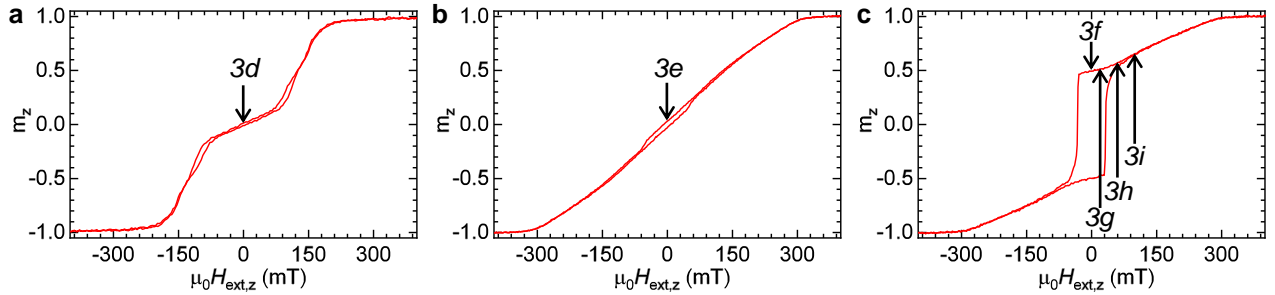


FIG. S5. Out-of-plane magnetization loops for **a.** SAF with effective PMA, **b.** SAF with vanishing effective PMA and **c.** BL-SAF. Lettered arrows indicate the field values at which images in corresponding Figure panels of the main part of the article have been obtained.

Supplementary Note 2 – Determination of bias coupling strengths

In order to determine the coupling field $\mu_0 H_{\text{bias}}$ between the BL and the SAF system as a function of the intermediate Pt layer thickness $t_{\text{Pt,BL}}$, we have elaborated an additional series of multilayers. Indeed, measuring a ferromagnetic coupling between two uniformly magnetized layers is more difficult than measuring an antiferromagnetic coupling (as we do for $\mu_0 H_{\text{RKKY}}$ inside the SAF), because any external field would reverse the whole structure without allowing a transition between antiferromagnetic and ferromagnetic configurations. Without such a transition, a determination of the ferromagnetic interlayer electronic coupling strength between two layers directly from magnetometry measurements is not achievable. As a consequence, a different multilayer structure is required, in which one of the two ferromagnetically coupled layers is blocked opposite to the applied field. We choose the structure $[\text{Co}(0.6 \text{ nm})/\text{Pt}(0.45 \text{ nm})]_3/\text{Co}(0.6 \text{ nm})/\text{Ru}(0.8 \text{ nm}) / [\text{Co}(0.6 \text{ nm})/\text{Pt}(0.45 \text{ nm})]_3/\text{Co}(0.6 \text{ nm})/\text{Pt}(t_{\text{Pt,BL}}) / \text{Co}(1.52\text{--}1.55 \text{ nm})/\text{Ru}(0.75 \text{ nm})$. It includes ferromagnetic coupling between a BL and a ferromagnetic layer through a Pt layer, identical to the BL and the bottom layer of the SAF of our targeted system. This BL is antiferromagnetically coupled to another BL through a Ru layer, constituting a common SAF structure, where $t_{\text{Ru}} = 0.8 \text{ nm}$ corresponds to the first peak of antiferromagnetic coupling in the absence of adjacent Pt layers. The thickness of the top Co layer is chosen slightly above 1.47 nm in order to get a linear, not hysteretic field evolution. Out-of-plane magnetization measurements are shown in Fig. S6.

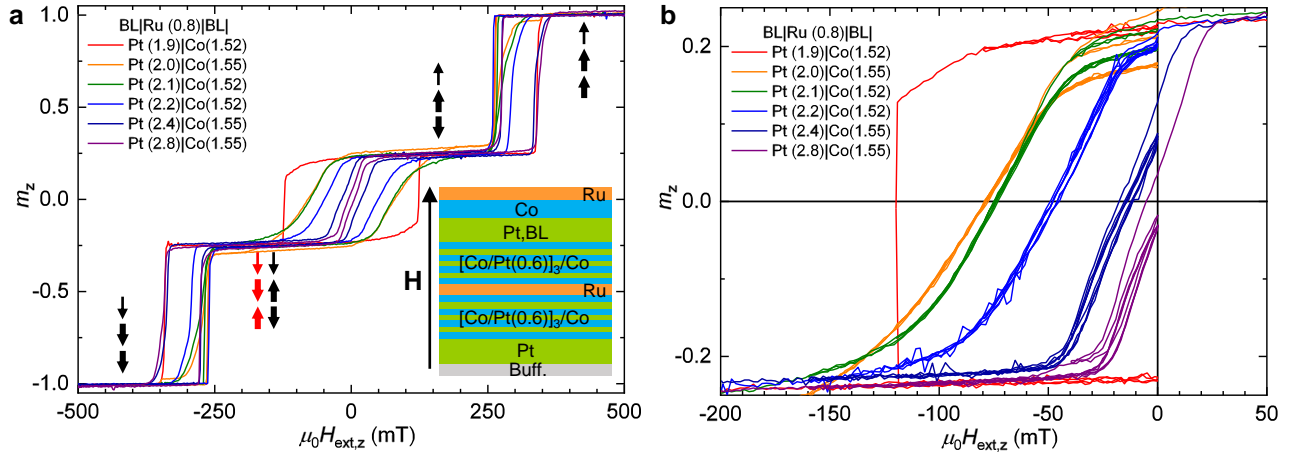


FIG. S6. Out-of-plane magnetization as a function of out-of-plane applied field for different values of $t_{\text{Pt,BL}}$ in a BL/Ru(0.8 nm)/BL/Pt($t_{\text{Pt,BL}}$)/Co(t_{Co}) multilayer structure. **a.** Full magnetization curves, where the magnetization configuration in the three layers for the different levels are described by the black sets of arrows. The red set of arrows depicts the magnetization configurations at the intermediate bottom level for the specific case of $t_{\text{Pt,BL}} = 1.9 \text{ nm}$ (too strong coupling). **b.** Minor magnetization switching loops of the top Co layer, allowing to extract $\mu_0 H_{\text{bias}}$.

As can be seen in Fig. S6a, both branches for increasing fields and decreasing fields exhibit three switching steps between four levels, corresponding to the successive switching of the two BLs and of the top Co layer. We describe, for example, the switching sequence for decreasing fields, as also indicated by the set of black arrows at each level. The first switching step corresponds to the bottom BL, under the action of the strong antiferromagnetic coupling to the other BL directly through Ru (and not the top BL, which also experiences a ferromagnetic coupling with the top Co layer that prevents it from switching first). The switching step corresponding to the FM is the central one, and occurs gradually due to absence of anisotropy. This step is actually shifted from zero by $\mu_0 H_{\text{bias}}$. The last switching step corresponds to the remaining BL. However, for a

too strong coupling, all layers in the structure suddenly switch before the top ferromagnetic layer reverses, as can be seen for $t_{\text{Pt,BL}} = 1.9$ nm (red set of arrows). This prevents us from measuring $\mu_0 H_{\text{bias}}$ for $t_{\text{Pt,BL}} < 2.0$ nm.

In order to extract more accurately the value of $\mu_0 H_{\text{bias}}$, we perform minor loops of the top Co layer switching, as shown in Fig. S6b. The field is initially decreased from saturation down to zero. Then, the field is reduced to negative field values, down to separate values 40 mT, 80 mT, 120 mT, 160 mT and 200 mT, but always coming back to zero field in between. This way, any coercivity of the top Co layer can be averaged out. We can extract the coupling field $\mu_0 H_{\text{bias}}$ as the central value of the different points where the magnetization crosses zero. The values of $\mu_0 H_{\text{bias}}$ that are obtained are all rescaled by $t_{\text{Co}}/1.47$ nm to find the expected coupling in the final BL-SAF systems.

Supplementary Note 3 – Spin-spirals period in SAF systems

Considering for simplicity an isotropic, single layer system uniform along the transverse direction (noted y), the energy per unit surface of the magnetization texture is given by

$$\epsilon = t_{\text{Co}} \left[A \sum_{i=x,y,z} \left(\frac{dm_i}{dx} \right)^2 + D \left(m_z \frac{dm_x}{dx} - m_x \frac{dm_z}{dx} \right) + K_{\text{eff}} (1 - m_z^2) + \Delta E_{\text{dip}} \right] \quad (1)$$

with t_{Co} the Co layer thickness, A the Heisenberg exchange parameter, D the DMI parameter, K_{eff} the effective perpendicular magnetic anisotropy of the system, and ΔE_{dip} , a correction related to long-range dipolar interactions. This correction is equal to $-\mu_0 M_s (\mathbf{m} \mathbf{H}_{\text{dip}} + M_s m_z^2) / 2$, the difference between energies found from dipolar fields \mathbf{H}_{dip} and the effective anisotropy approximation. For the system to form spontaneously spin-spirals, it is necessary that the DMI parameter D be larger than $D_c = \sqrt{A |K_{\text{eff}}|}$ [4]. Under this condition, the energy cost associated to varying magnetization for neighboring moments and rotation of the moments through the plane is compensated by the energy gain associated to chiral order. In general, the spin-spiral shows a non-regular rotation of the magnetization, due to the influence of the anisotropy that favors out-of plane ($K_{\text{eff}} > 0$) or in-plane ($K_{\text{eff}} < 0$) moments [4, 5]. For vanishing anisotropy and negligible dipolar interactions, the minimal energy state is a regular magnetic cycloid with Néel ordering. It is generally not observed in ferromagnetic materials, due to long-range dipolar interactions (ΔE_{dip}) that favor the formation of alternate magnetic domains, separated by chiral domain walls [5]. However, in our SAF system, the dipolar interactions are largely canceled out, owing to the antiferromagnetic ordering of the pair of magnetic layers. As the magnetization is only slowly varying in the spin-spirals (on a scale much longer than the magnetic layer spacing $p = 2.82$ nm), we have that $\Delta E_{\text{dip}} \approx 0$ due to the compensation of the magnetization. In our SAF system with vanishing anisotropy, we thus have a Néel ordering for which we can simplify (1) into

$$\epsilon = 2t_{\text{Co}} \left[A \left(\frac{dm_x}{dx} \right)^2 + A \left(\frac{dm_z}{dx} \right)^2 + D \left(m_z \frac{dm_x}{dx} - m_x \frac{dm_z}{dx} \right) \right], \quad (2)$$

whose solution found from variational approach is a cycloid of the form $[m_x, m_y, m_z] = [\cos(kx), 0, \pm \sin(kx)]$, depending on the sign of D [4]. The prefactor $2t_{\text{Co}}$ stands for the summation over the two antiferromagnetically coupled layers, which give identical energies, as one of the spin-spiral is simply shifted by half a period compared to the other. The RKKY coupling energy is zero in this model system, as all moments are perfectly antialigned. Using this solution, we can express the energy density of the cycloid state

$$\epsilon_k = \frac{k}{2\pi} \int_0^{2\pi/k} \epsilon dx = \frac{2kt_{\text{Co}}}{2\pi} \int_0^{2\pi/k} (k^2 A - kD) dx = 2t_{\text{Co}} (k^2 A - kD) \quad (3)$$

as a function of the characteristic period k . Minimizing this energy with respect to k yields $k = D/2A$, that is, a periodicity of $4\pi A/D$.

Supplementary Note 4 – Estimation of DMI

In order to estimate the value of the DMI in our final SAF system, we have deposited a series of multilayers with ferromagnetic interlayer coupling and varied repetition number, $[\text{Pt}(1.0\text{ nm})/\text{Co}(1.1\text{ nm})/\text{Ru}(1.4\text{ nm})]_{2,3,4,5,6}$, in order to perform domain size measurements [6–9]. The moderate number of layers deposited here allows to observe domains spacing, which is the consequence of a minimal energy balance between domain-domain dipolar interactions and domain walls formation, in a regime for which domain walls are well separated from each other. In this series of multilayers, the DMI is strong enough compared to dipolar interactions and ensures a uniform chirality of the domain walls through the multilayer thickness, thus greatly simplifying the analysis of the domains spacing [9]. Therefore, we can use the analytical model of Lemesh *et al.* [8] to deduce micromagnetic parameters from domain sizes, which is based on a set of three variables: stripe domains periodicity (λ), domain wall width (Δ) and domain wall internal angle (ϕ , always corresponding to Néel walls here). Assuming $A = 10\text{ pJ m}^{-1}$ [6], we can find the domain wall energies and thus the DMI values that correspond to the observed domains spacing, which are listed in Table S6. For this series of samples, a best fit for saturation magnetization M_s with experimental domains spacing dependence on N results in $M_s = 0.975 \pm 0.075\text{ MA m}^{-1}$. The reduction of M_s compared to our thicker SAF samples originates in Co layer thickness reduction and thicker Ru layer. We measured an in-plane saturation field $\mu_0 H_{\text{eff}} = 520\text{ mT}$, corresponding to $K_{\text{eff}} = 0.254\text{ MJ m}^{-3}$. We obtain an average DMI magnitude $D = 1.02\text{ mJ m}^{-2}$. Conversely, the interface DMI parameter is found as $D_s = 1.12\text{ pJ m}^{-1}$, which gives $D = 0.76\text{ mJ m}^{-2}$ in our SAF system with $t_{\text{Co}} = 1.47\text{ nm}$ if an inverse dependence on Co layer thickness is strictly observed.

TABLE S6. Summary of domain spacing measurements in the $[\text{Pt}(1.0\text{ nm})/\text{Co}(1.1\text{ nm})/\text{Ru}(1.4\text{ nm})]_N$ series. The number of repetitions of the magnetic layer N , measured domains periodicity λ and DMI amplitude D are given for each multilayer.

Multilayer stack	N	λ (nm)	D (mJ m^{-2})
$[\text{Pt}(1.0\text{ nm})/\text{Co}(1.1\text{ nm})/\text{Ru}(1.4\text{ nm})]_2$	2	2500 ± 312	1.11 ± 0.12
$[\text{Pt}(1.0\text{ nm})/\text{Co}(1.1\text{ nm})/\text{Ru}(1.4\text{ nm})]_3$	3	1130 ± 59	1.00 ± 0.14
$[\text{Pt}(1.0\text{ nm})/\text{Co}(1.1\text{ nm})/\text{Ru}(1.4\text{ nm})]_4$	4	600 ± 37	1.02 ± 0.14
$[\text{Pt}(1.0\text{ nm})/\text{Co}(1.1\text{ nm})/\text{Ru}(1.4\text{ nm})]_5$	5	482 ± 23	0.96 ± 0.14
$[\text{Pt}(1.0\text{ nm})/\text{Co}(1.1\text{ nm})/\text{Ru}(1.4\text{ nm})]_6$	6	365 ± 14	1.02 ± 0.15

Supplementary Note 5 – Additional MFM observations: demagnetized BL, saturated BL, domains in a single layer, and uniform SAF

We provide here a series of supplementary MFM images, recorded on the different multilayer components that were used to build the BL-SAF of the main part of the article. First, in order to verify whether the observed MFM signal could originate in ferromagnetic domains remaining inside the BL, some images of the BL alone (deposited without a SAF on top) have been recorded under identical imaging conditions, after demagnetization of the BL. Its magnetization is hence non-uniform and presents perpendicularly magnetized domains. An example of image is shown in Fig. S7a, which reveals domains with a very large contrast, more than one order of magnitude larger than the contrast observed in the BL-SAF system after saturation of the BL. Even for the small and isolated circular domain present in the top-right part of the image, the height of the 200 nm-large profile is as large as 12° , incompatible with the contrast level observed in the SAF system with saturated BL, which must have a different origin. This proves that in the MFM images presented in the main part of the article (see Fig. 3), the BL remains uniformly saturated at zero field, and that we image the configuration of the SAF system only.

Next, in order to verify that the observed MFM signal does originate from ferromagnetic skyrmions stabilized in only one layer of the SAF, some images of a single magnetic layer (Pt/Co(1.47 nm)/Ru/Pt) have been recorded for identical imaging conditions when the Co layer has been demagnetized and thus presents large magnetic domains, due to magnetostatic equilibrium under dipolar interactions. Imaging with the same tip used for the other images, the domains are erased due to their interaction with the magnetic moment the tip. Despite the resulting perturbations on the images, a contrast level of around 15° is observed. In order to obtain a satisfying, less perturbed image as the one shown in Fig. S7b, we had to rely on a magnetic tip with a magnetic coating 8 times thinner than the one used for the images of the BL-SAF system (see Table S7). With this different tip, a contrast level of 2° is observed, consistent with the previous value of 15° divided by 8. For the tip used to image the BL-SAF, the observed contrast level and expected tip perturbation effects are thus incompatible with ferromagnetic skyrmions stabilized in only one layer of the SAF.

In Fig. S7c, we display an image of the BL alone, deposited without a SAF on top, after saturation under external field. In Fig. S7d, we present an image that has been recorded at the inner of a single domain of the SAF system with large anisotropy (far from the antiferromagnetic domain walls), without BL. Both images of the saturated systems feature some background signal, ranging a few tenths of a degree, which may be attributed to roughness or small thickness fluctuations of the layers, but which corresponds to a uniform BL and to a uniform magnetic configuration in the SAF, respectively, for Fig. S7c and Fig. S7d. This is to be linked to the background that can be observed around the antiferromagnetic skyrmions in the BL-SAF system.

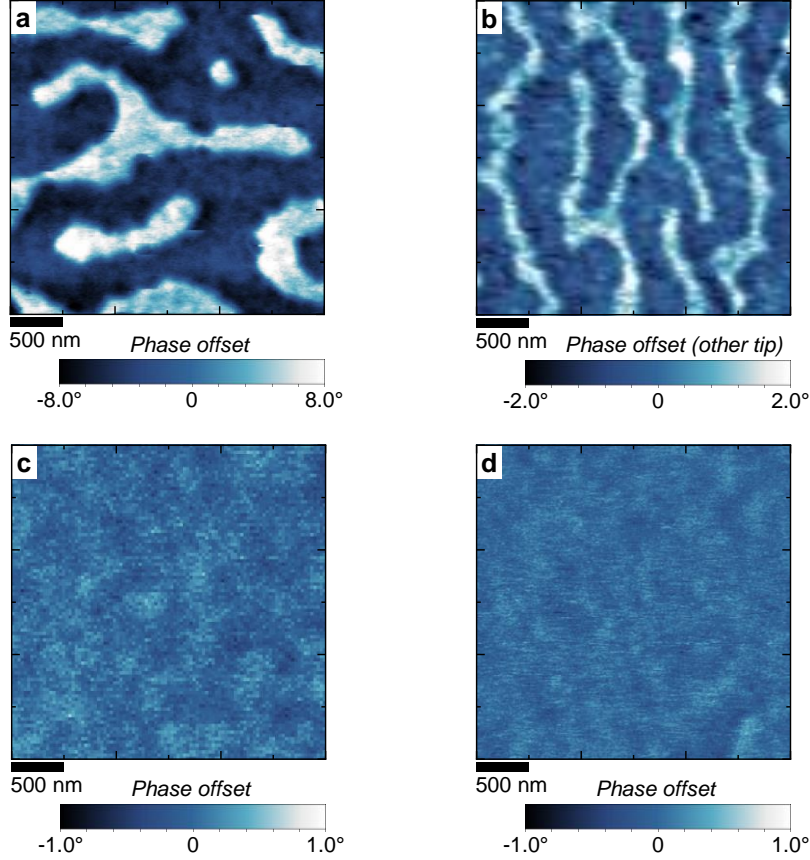


FIG. S7. MFM observations of additional magnetization structures. **a.** MFM image of demagnetized BL at $\mu_0 H_{\text{ext}} = 0$ mT. A very large contrast, one order of magnitude larger than before, is obtained for domains located in the BL. Notably, the height of the peak for the small circular domain located in the top right part is 12° . **b.** MFM image of a demagnetized single Co layer at $\mu_0 H_{\text{ext}} = 0$ mT. This image has been obtained with a tip having an 8 times thinner magnetic coating, which hence provides 8 times smaller signal than the tip used before, in order to avoid too strong perturbation by interaction with the magnetic domains. **c.** MFM image of a BL alone, after saturation under field and back to $\mu_0 H_{\text{ext}} = 0$ mT. **d.** MFM image of a uniform domain of a SAF with large anisotropy at $\mu_0 H_{\text{ext}} = 0$ mT. A small background signal is observable even for these saturated multilayers.

Supplementary Note 6 – Quantitative study of the MFM signal of the antiferromagnetic skyrmions as a function of external field

In this section, we analyze quantitatively the MFM signal obtained from the antiferromagnetic skyrmions, in the series of images recorded at different external fields (Figs. 3g–i) recorded on the BL-SAF system hosting antiferromagnetic skyrmions of the main part of the article. For these supplementary images, a perpendicular magnetic field is now applied to the multilayer during imaging, $\mu_0 H_{\text{ext}} = 20$ mT (Fig. 3g), 60 mT (Fig. 3h) and 100 mT (Fig. 3i), instead of imaging at zero field. First, at 20 mT, the contrast observed inside the black spots increases compared to what is seen at zero field. As we see below, this enhancement is due to the slight deformation of the skyrmion profiles in the two layers of the SAF, thus enlarging the outgoing stray field. Then at 60 mT, the contrast is even further enhanced, and correspondingly the magnetic configuration becomes sensitive to the magnetization of the tip, as can be seen from the top-left skyrmion, which is perturbed by tip interaction during imaging. Finally at 100 mT, the black dots have disappeared, which we can understand as the annihilation of the antiferromagnetic skyrmions once the RKKY field is overcome by the external field.

In MFM experiments, the tip can be very similar to either a magnetic monopole located at its apex or to a magnetic dipole located in the tip, depending on the characteristic dimensions of the stray field compared to the dimensions of the tip [10]. Because for the present antiferromagnetic structures in SAF systems the decay length of the magnetic signal is much shorter than the tip vertical dimension, the magnetic monopole model is most suitable (note that we have also performed modeling of the MFM signal within the dipole model, which instead provides inconsistent results). The tip is aligned along the vertical direction in our setup, which thus makes it sensitive to vertical gradients of the stray field vertical component, $\mu_0 dH_z/dz$. However, the oscillating motion of the tip during imaging needs to be considered. In MFM experiments in double pass, tapping mode, the cantilever that holds the tip oscillates in a forced regime during the scan, allowing to relate the force exerted by the field gradient to a phase shift in the detected signal. As a consequence, the probing volume of the tip is not only its own volume, but its moving volume during oscillations. The expected field gradient map has to be convoluted with the probing profile of the oscillating tip to get the expected signal. As the tip oscillates in sinusoidal fashion, the time spent at different z locations varies with position z ; specifically, more time is spent at the extremities, which, fortunately, enhances the sensitivity as there are stronger gradients close to the multilayer surface. Therefore, such vertical spatial average needs to be calculated with a weight function being the inverse of the sinusoidal oscillations, hence proportional to the arcsine function, as represented in Fig. S8. Moreover, the finite size of the sensitive part at the MFM tip apex (in the range of a few tens of nm) has to be considered. The bare tip has an estimated radius of curvature of 10 nm. Specifically, for a tip with 23 nm of FM layer CoFeB deposited as a coating, there is thus an estimated radius of curvature of around 30 nm for the magnetic part of the tip. Table S7 below reports tip characteristics and imaging conditions, with the free oscillation amplitude of each tip set at 340 nm (peak to peak). The different drive amplitude during the second pass of the tip (lift mode), the thickness of the magnetic and of the non-magnetic capping layers deposited on the tip are taken into account to determine the oscillation window of the position of the equivalent magnetic monopole at the tip apex, relative to the surface of the sample. In order to be quantitative, each tip is used with a unique set of imaging parameters, and only images recorded with a single tip can be compared, as even nominally identical tips may result in different signal levels due to shape variations, cantilever resonance quality factor difference, etc.

In order to predict the MFM signal expected from the antiferromagnetic skyrmions at different external field values, we first need to determine the tip sensitivity, that is, the factor of conversion between $\mu_0 dH_z/dz$ (in T m^{-1}) and phase offset in lift mode (in $^\circ$). To do this, we rely on the

TABLE S7. Summary of magnetic tips used for quantitative MFM measurements. In order to be quantitative, each tip is used with a unique set of imaging parameters. Magnetic coating thickness, tapping oscillation amplitude (during first pass), lift oscillation amplitude (during second pass), lift height, deduced oscillation window of the tip monopole and corresponding images are given for each tip.

Tip #	Coating (nm)	1 st pass ampl. (nm)	2 nd pass ampl. (nm)	Lift height (nm)	Oscillation window (nm)	Figs.
1	3 nm magn. + 10 nm non-magn.	237	170	0	45–215	S7b
2	7 nm magn. + 10 nm non-magn.	220	113	0	67–180	3e
3	23 nm magn. + 10 nm non-magn.	237	170	0	55–225	3d,f–i; S7a,c,d;

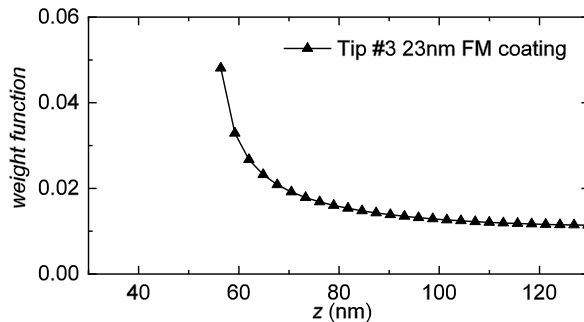


FIG. S8. Weight function corresponding to averaging vertically the field gradient taking into account the oscillations of tip #3, where the weight is proportional to time spent at position z during an oscillation.

images of the spin-spirals, as they have a well-defined periodicity that is observed by MFM. Their periodicity imposes the spin-spiral profile, which shall then only weakly depend on the magnetic parameters, and hence can be used as a reliable model system. We first predict this magnetization profile of the spin-spirals (Fig. S13), the generated stray field (Fig. S14) and the map of vertical field gradient (Fig. S15) expected from them, in Note 7. Then, at each position x , the magnetic signal is determined as the average field gradient $\langle \mu_0 dH_z/dz \rangle$ from the z -profile of $\mu_0 dH_z/dz$, weighted by the function of Fig. S8, which results in the dark line MFM signal profile displayed in Fig. S9. For example, the value at $x = 0$ is found as the cumulative product of Fig. S15e multiplied by Fig. S8. Finally, this ideal MFM profile is convoluted with a 60 nm window in order to approximate the limit to the resolution caused by the finite probe size, which results in our final prediction for the MFM signal expected from these magnetic textures (red line profile displayed in Fig. S9). Note that a tip different than tip #3 had to be used to image satisfyingly the system shown in Fig. 3e, because the spin-spiral appeared softer than other textures and was easily perturbed by the tip. Nevertheless, we could also record line profiles in unperturbed parts of the image of the spin-spiral configuration with tip #3, as shown in Fig. S11a, providing in this case a contrast level of about $\pm 0.75^\circ$ (instead of $\pm 0.45^\circ$ with tip #2). This calibration on the spin-spiral configuration of the sensitivity of tip #3 provides 0.75° for an average gradient of $8.15 \mu\text{T nm}^{-1}$, that is, $0.092^\circ \text{ nm } \mu\text{T}^{-1}$ for this tip.

To validate our model of stray field and MFM signal prediction, we check that the MFM signal recorded on the antiferromagnetic domain walls in the main part of the article (Fig. 3d) indeed matches the signal that can be predicted by micromagnetic simulations. Following the same procedure as just above, we predict the domain wall magnetization profile (Fig. S16), the generated stray field (Fig. S17) and the map of vertical field gradient (Fig. S18) expected from it, in Note 7. Then, at each position x , the magnetic signal is determined as the average field gradient $\langle \mu_0 dH_z/dz \rangle$ from the z -profile of $\mu_0 dH_z/dz$, weighted by the function of Fig. S8, which

results in the dark line MFM signal profile displayed in Fig. S10. Finally, this ideal MFM profile is convoluted with the 60 nm window in order to approximate the limit to the resolution caused by the finite probe size, which results in our final prediction for the MFM signal expected from the antiferromagnetic domain walls observed in Fig. 3d (red line profile displayed in Fig. S10). The corresponding line profiles for the MFM signal generated by the domain walls present in Fig. 3d, indeed recorded with tip #3, are drawn in Fig. S11b, providing in this case a contrast level of about $\pm 0.5^\circ$. This result is fully consistent with the previously determined sensitivity of tip #3, as 0.5° for an average gradient of $5.53 \mu\text{T nm}^{-1}$ now provides around $0.090^\circ \text{ nm } \mu\text{T}^{-1}$, the difference with $0.092^\circ \text{ nm } \mu\text{T}^{-1}$ being below the noise level here.

Similar as with spin-spirals and domain walls, we can now predict the magnetization profiles of the isolated antiferromagnetic skyrmions under different external fields (Fig. S19), and in each case the generated stray field (Figs. S20–S22a,b) and the map of vertical field gradient (Figs. S20–S22c) expected from them, in Note 8. Then, at each radial position r , the magnetic signal is determined from the z -profile of $\mu_0 dH_z/dz$ as the average field gradient $\langle \mu_0 dH_z/dz \rangle$, weighted by the function of Fig. S8, which results in the dark line MFM signal profiles displayed in Figs. S20–S22d. Again, these ideal MFM profiles are convoluted in two dimensions with a 60 nm square window in order to approximate the limit to the resolution caused by the finite probe size, which results in our prediction for the MFM signal expected with tip #3 from these antiferromagnetic skyrmion textures (red line profiles displayed in Figs. S20–S22d). Finally, we perform Gaussian fits to these signal peaks, similar to what has been performed for our MFM experimental data (dashed blue line profiles displayed in Figs. S20–S22d).

We can now verify how the predicted signal compares with our MFM data. As shown in Fig. S12a by comparing the Gaussian fits of the signal peaks, in the MFM experimental data (colored dots) and in the calculations (blue lines), the contrast levels match exceptionally well. A good agreement is also found for the evolution of the apparent skyrmion size (Fig. S12b), despite some systematic underestimation. We believe that this difference is due to an additional enlargement of the skyrmion size, because of its interaction with the moment of the magnetic tip during imaging, an effect that cannot be easily modeled.

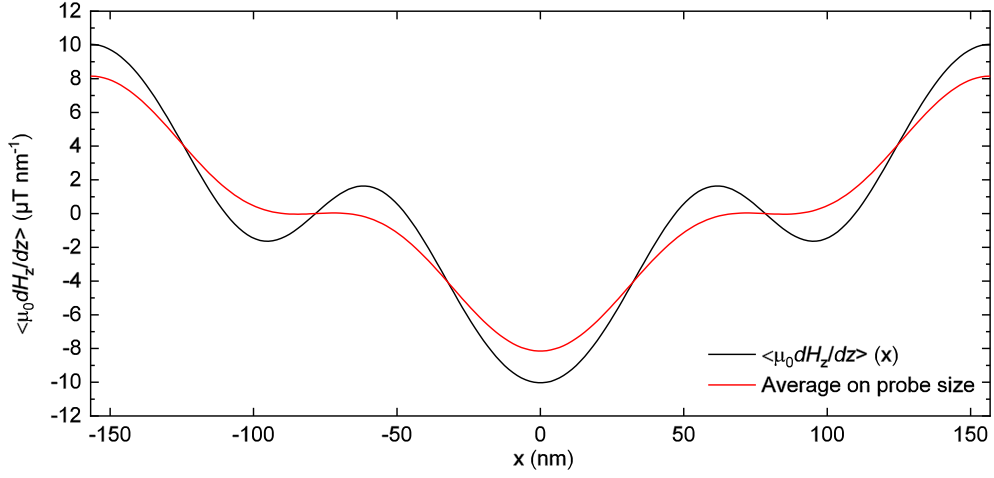


FIG. S9. For the spin-spiral configuration of Note 7, field vertical gradient probed by the tip averaged for vertical tip oscillations (black line), and averaged horizontally to take into account tip size of around 60 nm as a limit to the resolution (red line).

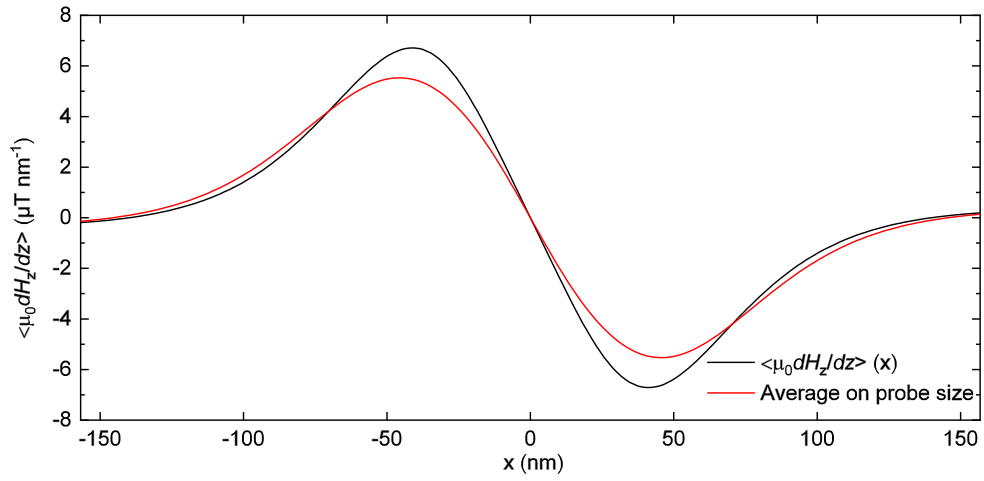


FIG. S10. For the domain wall configuration of Note 7, field vertical gradient probed by the tip averaged for vertical tip oscillations (black line), and averaged horizontally to take into account tip size of around 60 nm as a limit to the resolution (red line).

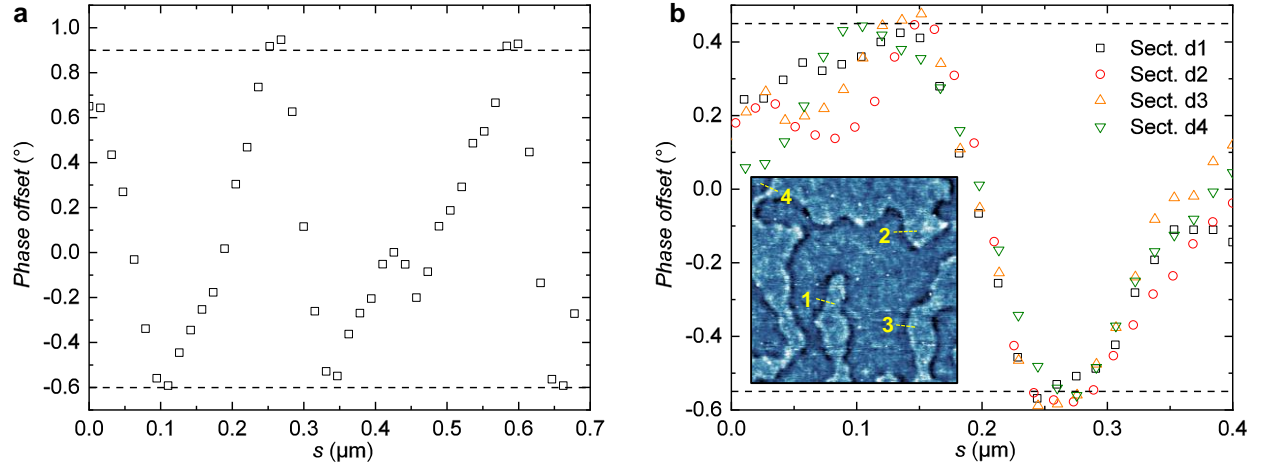


FIG. S11. **a.** For the SAF system hosting the spin-spirals, line section of the MFM signal (phase offset in lift mode) recorded with tip #3. **b.** For the SAF system hosting domain walls, line sections d1, d2, d3 and d4 of the MFM signal (phase offset in lift mode) recorded in the image of Fig. 3d (using tip #3 as well). Inset in panel b indicates the location of the line sections.

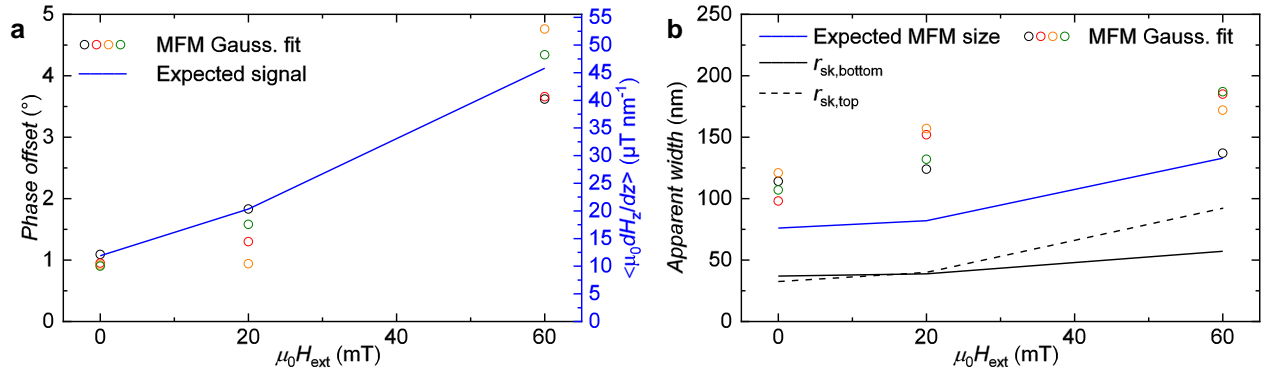


FIG. S12. **a,b.** Comparison of contrast level (a) and apparent skyrmion diameter (b) between calculations (blue lines) and MFM data (colored dots). Black lines in panel b correspond to skyrmion diameters, reported from Fig. S19.

Supplementary Note 7 – Stray field predicted for antiferromagnetic spin-spirals and domain walls in SAF systems

In this section, we predict the expected profile and associated measurable fields and their derivatives for antiferromagnetic spin-spirals and domain walls in SAF systems. Using the experimentally determined magnetic parameters, the expected spin-spiral magnetization profile in each layer is obtained by energy minimization in the MuMax³ micromagnetic simulation code. The result is displayed in Fig. S13, which reveals a slight deformation of the profiles compared to sinusoids due to a small influence of intralayer dipolar fields. This allows to compute the expected stray field above the spin-spiral, whose spatial map is reported in Fig. S14. We analyze separately the horizontal component H_x (Fig. S14a) and the vertical component H_z (Fig. S14b). By computing the vertical gradient of the vertical component dH_z/dz (Fig. S15), we access the physical quantity that is probed by the MFM experiment. Predicting the expected MFM signal still requires averaging, as performed in Note 6.

Using the same experimentally determined magnetic parameters, except including now $\mu_0 H_{\text{eff}} = 60 \text{ mT}$ for $t_{\text{Co}} = 1.41 \text{ nm}$ instead of zero effective anisotropy, the expected domain wall magnetization profile in each layer is obtained also by energy minimization in the MuMax³ micromagnetic simulation code. The result is displayed in Fig. S16 and reveals, as expected, a much faster rotation of the magnetization than in the spin-spiral. This profile allows to compute the expected stray field above the domain wall, whose spatial map is reported in Fig. S17. We analyze separately the horizontal component H_x (Fig. S17a) and the vertical component H_z (Fig. S17b). By computing the vertical gradient of the vertical component dH_z/dz (Fig. S18), we access the physical quantity that is probed by the MFM experiment. Predicting the expected MFM signal still requires averaging, as performed in Note 6.

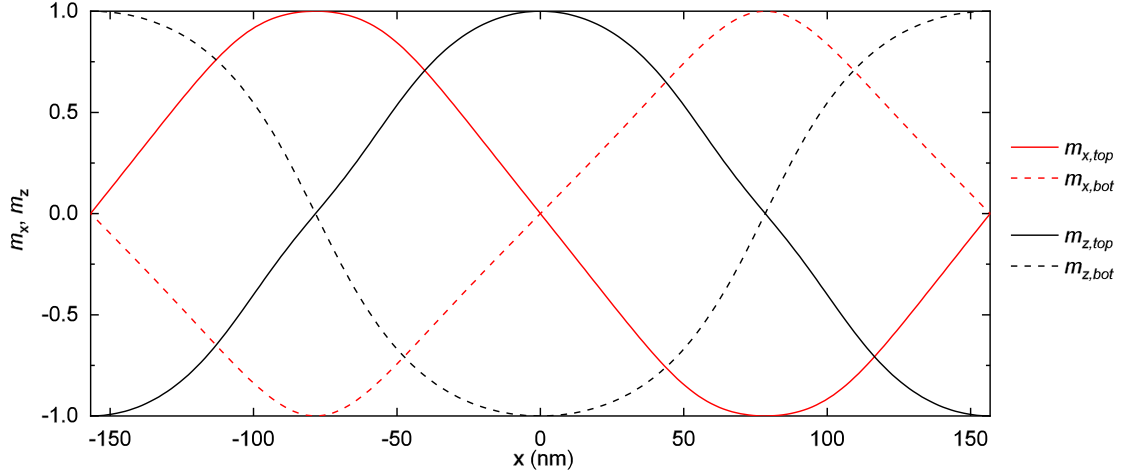


FIG. S13. Magnetic profile of the spin-spiral configuration over one period. Solid lines correspond to top layer, dashed lines to bottom layer. Red lines correspond to the horizontal component m_x , black lines to the vertical component m_z of the magnetization.

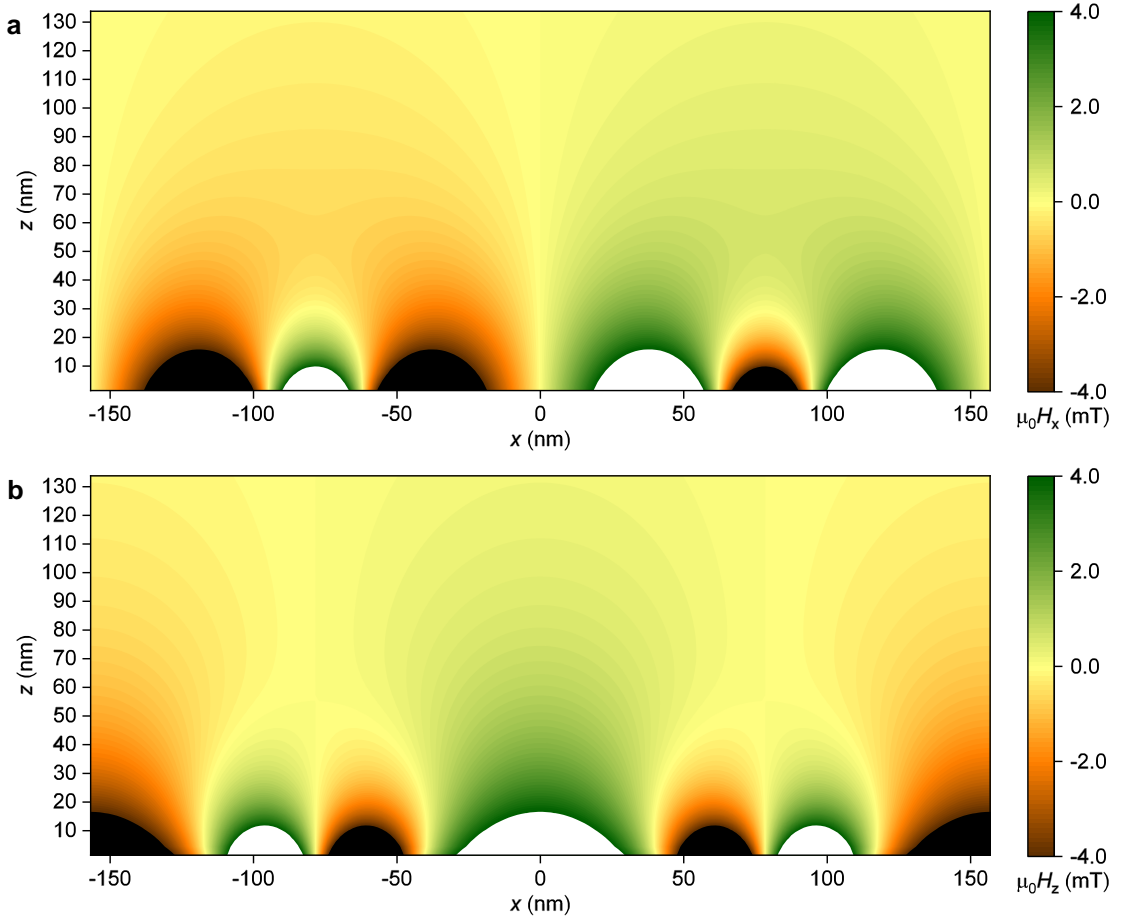


FIG. S14. Color maps of the stray field generated by antiferromagnetic spin-spirals in SAF systems. **a,b.** Horizontal component (a) and vertical component (b) of the stray field for a period of the antiferromagnetic spin-spiral, encoded according to the colorscale given on the right. White (black) color corresponds to fields larger (lower) than 4 mT (-4 mT).

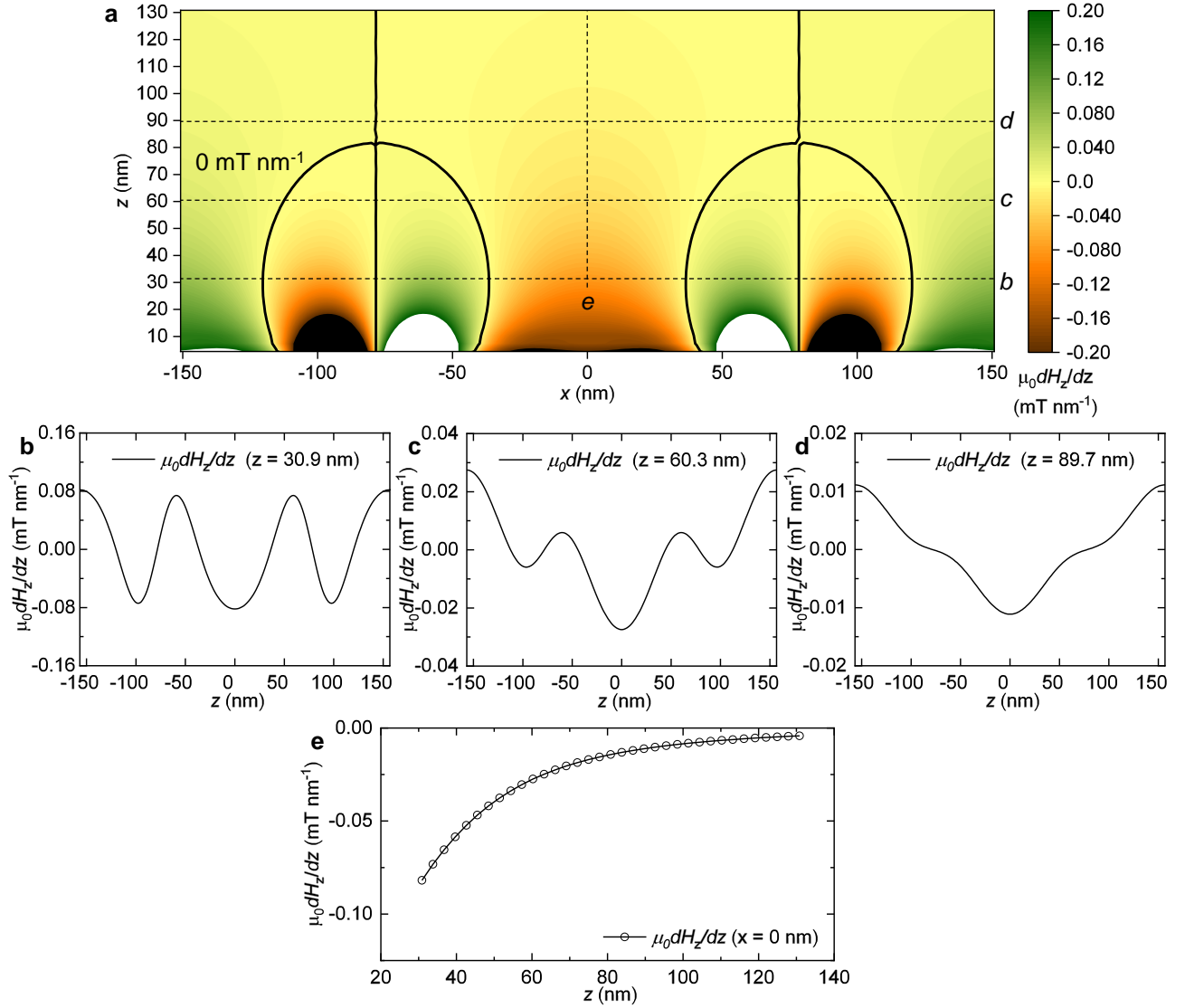


FIG. S15. Stray field gradient generated by antiferromagnetic spin-spirals in SAF systems. **a.** Color map of the first partial z -derivative of the vertical component of the stray field for a period of the antiferromagnetic spin-spiral, encoded according to the colorscale given on the right. White (black) color corresponds to field gradients larger (lower) than 0.20 mT nm^{-1} (-0.20 mT nm^{-1}). Thick black line indicates where $\mu_0 dH_z/dz = 0$. Thin dashed lines indicate the cuts that are displayed in the following lettered panels. **b–d.** Horizontal cuts of the field gradient at $z = 30.9$ nm (**b**), $z = 60.3$ nm (**c**), and $z = 89.7$ nm (**d**). **e.** Vertical cut of the field gradient at $x = 0$, revealing the expected fast decay with elevation.

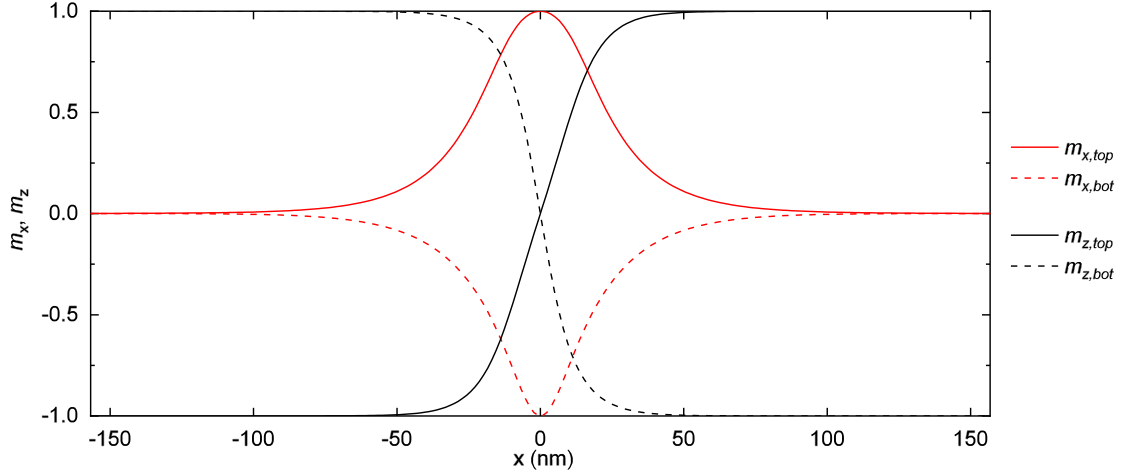


FIG. S16. Magnetic profile of the domain wall configuration. Solid lines correspond to top layer, dashed lines to bottom layer. Red lines correspond to the horizontal component m_x , black lines to the vertical component m_z of the magnetization.

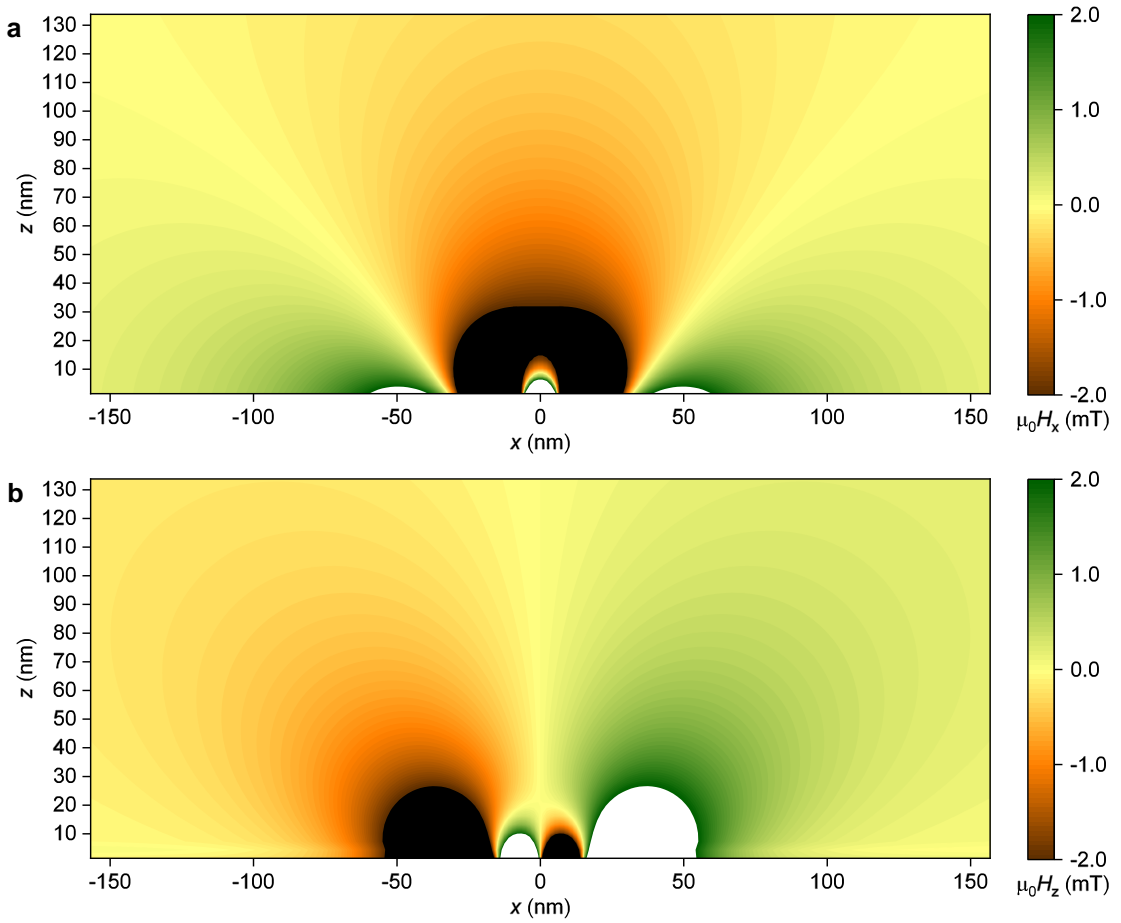


FIG. S17. Color maps of the stray field generated by an antiferromagnetic domain wall in the SAF system. **a,b.** Horizontal component (a) and vertical component (b) of the stray field as seen at both sides of the domain wall, encoded according to the colorscale given on the right. White (black) color corresponds to fields larger (lower) than 2 mT (-2 mT).

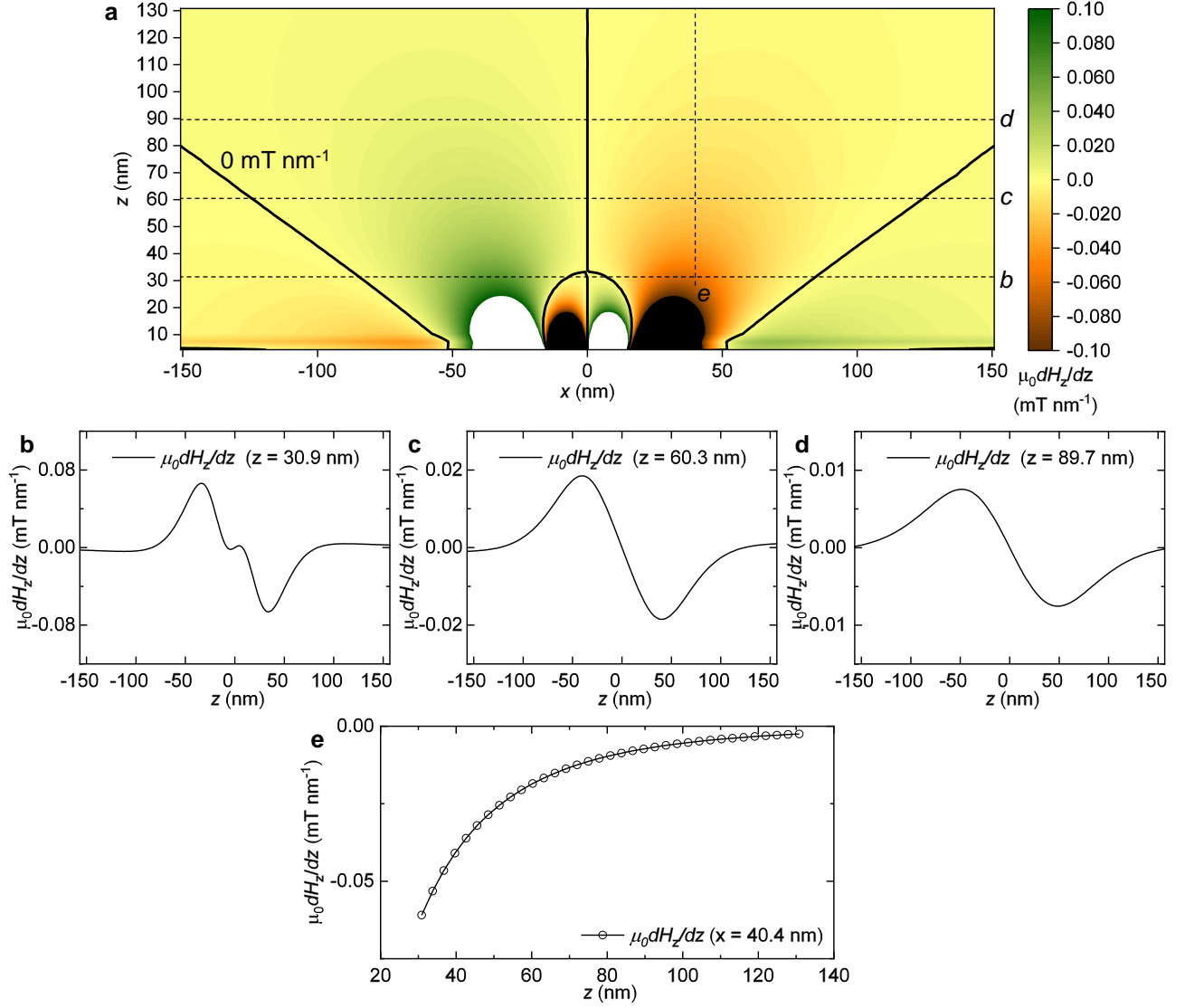


FIG. S18. Stray field gradient generated by an antiferromagnetic domain wall in the SAF system. **a.** Color map of the first partial z -derivative of the vertical component of the stray field as seen at both sides of the domain wall, encoded according to the colorscale given on the right. White (black) color corresponds to field gradients larger (lower) than 0.10 mT nm^{-1} (-0.10 mT nm^{-1}). Thick black line indicates where $\mu_0 dH_z/dz = 0$. Thin dashed lines indicate the cuts that are displayed in the following lettered panels. **b–d.** Horizontal cuts of the field gradient at $z = 30.9$ nm (b), $z = 60.3$ nm (c), and $z = 89.7$ nm (d). **e.** Vertical cut of the field gradient at $x = 40.4$ nm, revealing the expected fast decay with elevation.

Supplementary Note 8 – Stray field and MFM signal predicted for antiferromagnetic skyrmions in SAF systems

In order to get a better understanding of the MFM images provided by antiferromagnetic skyrmions in SAF systems, we use our micromagnetic model [11] to predict the expected measurable fields and their derivatives (see section on micromagnetic modeling in the Methods part of the article). We determine the equilibrium skyrmion profiles by energy minimization for the experimentally determined $D = 0.5 \text{ mJ m}^{-2}$ and $\mu_0 H_{\text{bias}} = 50 \text{ mT}$. The equilibrium radii in the bottom and top layers at $\mu_0 H_{\text{ext}} = 0 \text{ mT}$ are 18.4 nm and 16.2 nm, respectively. We display, in Fig. S19a, the evolution with the external magnetic field of the skyrmion profile in the SAF, and in Fig. S19b, the evolution of the skyrmion radii. It appears that under an external magnetic field, the skyrmion radius in the top layer expands much more than the skyrmion radius of the bottom layer, causing decompensation of the total magnetization of the two layers.

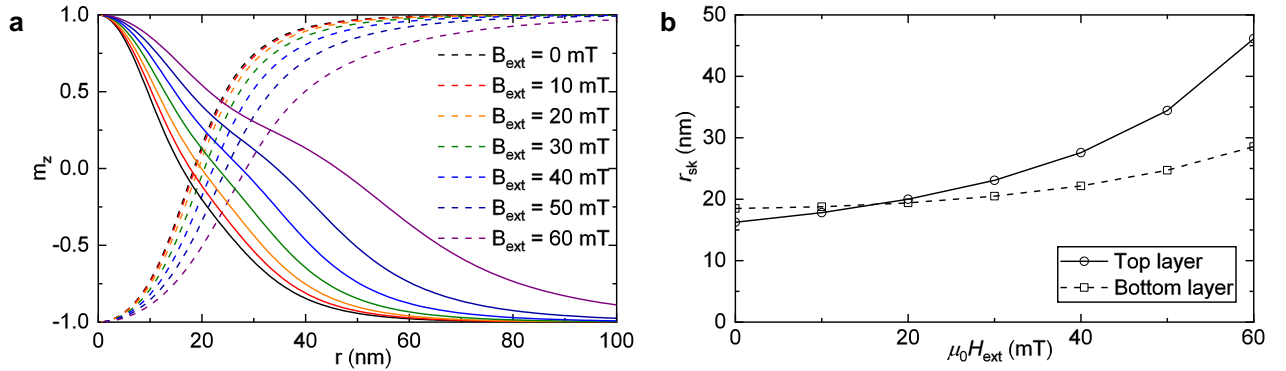


FIG. S19. Simulated field-dependence of an antiferromagnetic skyrmion in the SAF system. **a.** Radial profiles of the vertical magnetization component m_z of the skyrmion for $\mu_0 H_{\text{ext}} = 0\text{--}60 \text{ mT}$ with $D = 0.5 \text{ mJ m}^{-2}$ and $\mu_0 H_{\text{bias}} = 50 \text{ mT}$. Top layer profiles are the solid lines, while bottom layer profiles are the dashed lines. **b.** Evolution of r_{sk} in the top and bottom layer as a function of $\mu_0 H_{\text{ext}}$.

Using the same method as to determine the dipolar fields inside the magnetic system, we are able to get the stray field at arbitrary heights above the system. We report in Figs. S20, S21 and S22 radial maps of the stray field above the antiferromagnetic skyrmions. We analyze separately the radial component H_r (Figs. S20–S22a) and the vertical component H_z (Figs. S20–S22b) of the stray field. Because the antiferromagnetic order partially cancels the stray field, its decay with distance from the skyrmion is expected to be faster than for usual ferromagnetic skyrmions. For these antiferromagnetic skyrmions, the magnetic profile hosted in the top layer is located closer to the tip, which generates positive fields on top of the antiferromagnetic skyrmion (dark contrast in our setup), in the direction of the saturated BL. By computing the vertical gradient of the vertical component dH_z/dz (Figs. S20–S22c), we access the physical quantity that is probed by the MFM experiment.

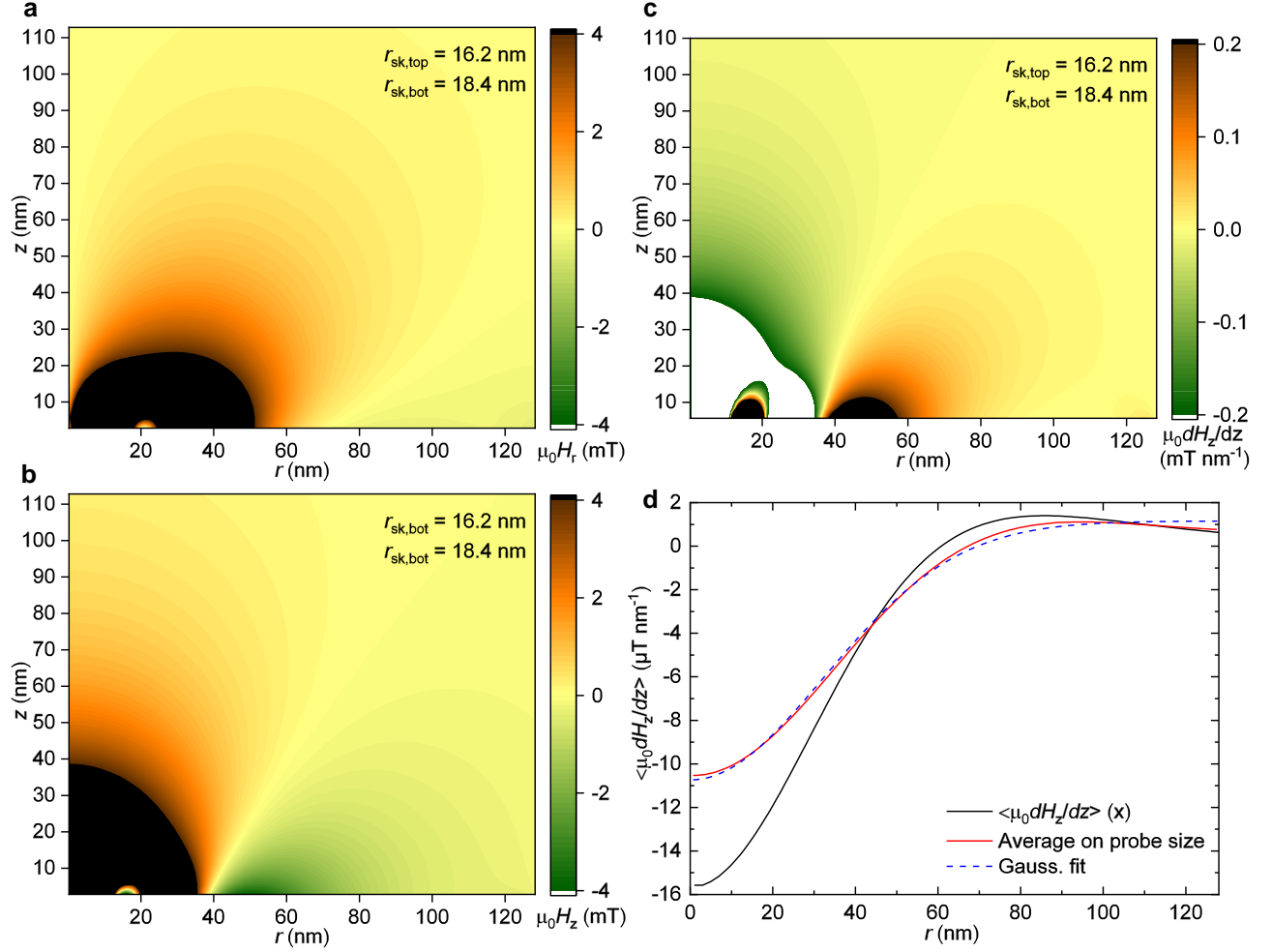


FIG. S20. Stray field generated by an antiferromagnetic skyrmion in the BL-SAF at $\mu_0 H_{\text{ext}} = 0$ mT. **a–c.** Color maps of radial component (a), vertical component (b), and first partial z -derivative of the vertical component (c) of the stray field, encoded according to the colorscale given on the right. White (black) color corresponds to fields or field gradients larger (lower) than 4 mT or 0.20 mT nm^{-1} (-4 mT or -0.20 mT nm^{-1}). **d.** Field vertical gradient probed by the tip, averaged for tip oscillations (black line), and then averaged horizontally to take into account tip size of around 60 nm as a limit to the resolution (red line), and fit of this expected signal shape to a Gaussian peak function (dashed blue line).

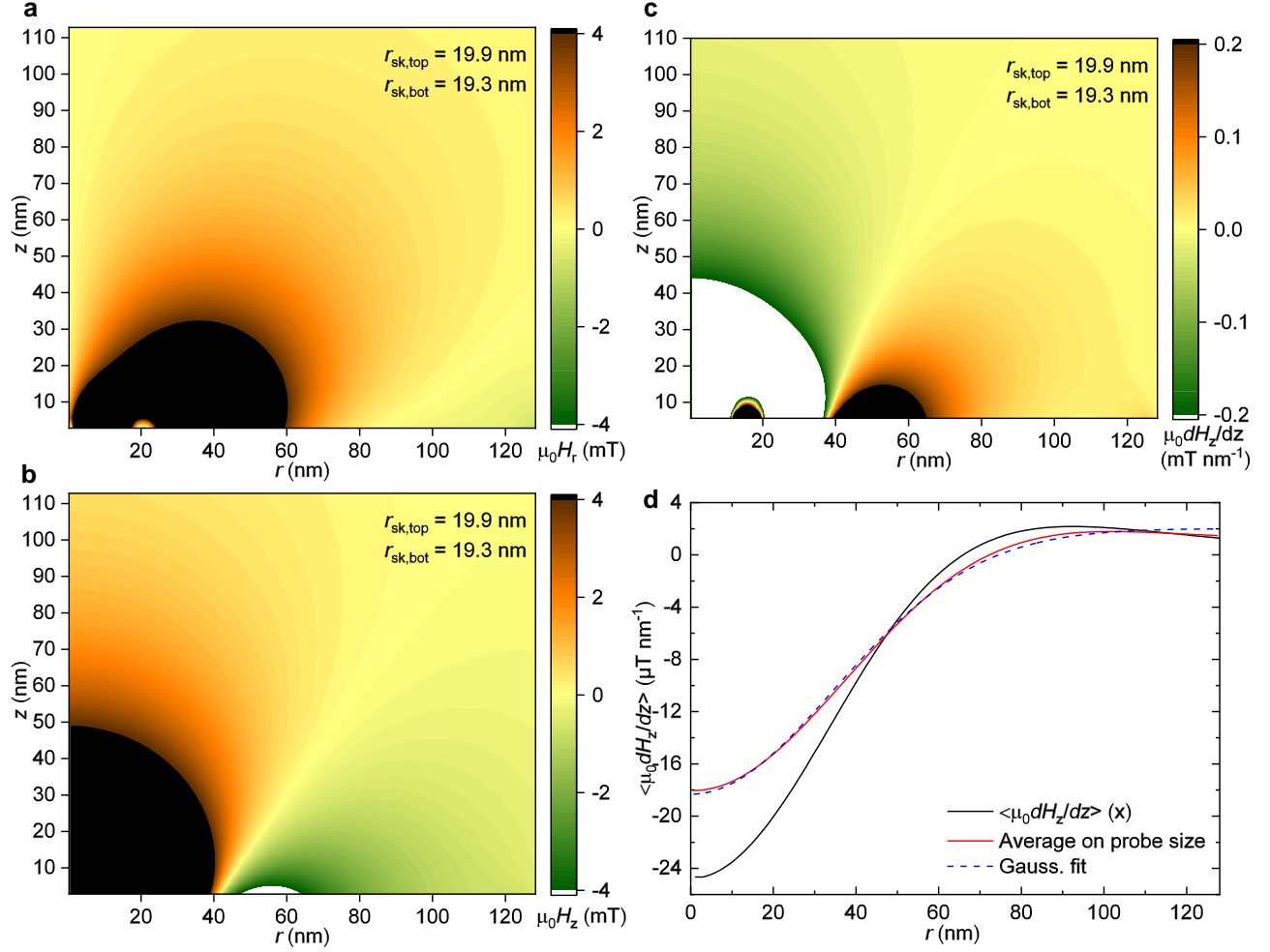


FIG. S21. Stray field generated by an antiferromagnetic skyrmion in the BL-SAF at $\mu_0 H_{\text{ext}} = 20$ mT. **a–c.** Color maps of radial component (a), vertical component (b), and first partial z -derivative of the vertical component (c) of the stray field, encoded according to the colorscale given on the right. White (black) color corresponds to fields or field gradients larger (lower) than 4 mT or 0.20 mT nm^{-1} (-4 mT or -0.20 mT nm^{-1}). **d.** Field vertical gradient probed by the tip, averaged for tip oscillations (black line), and then averaged horizontally to take into account tip size of around 60 nm as a limit to the resolution (red line), and fit of this expected signal shape to a Gaussian peak function (dashed blue line).

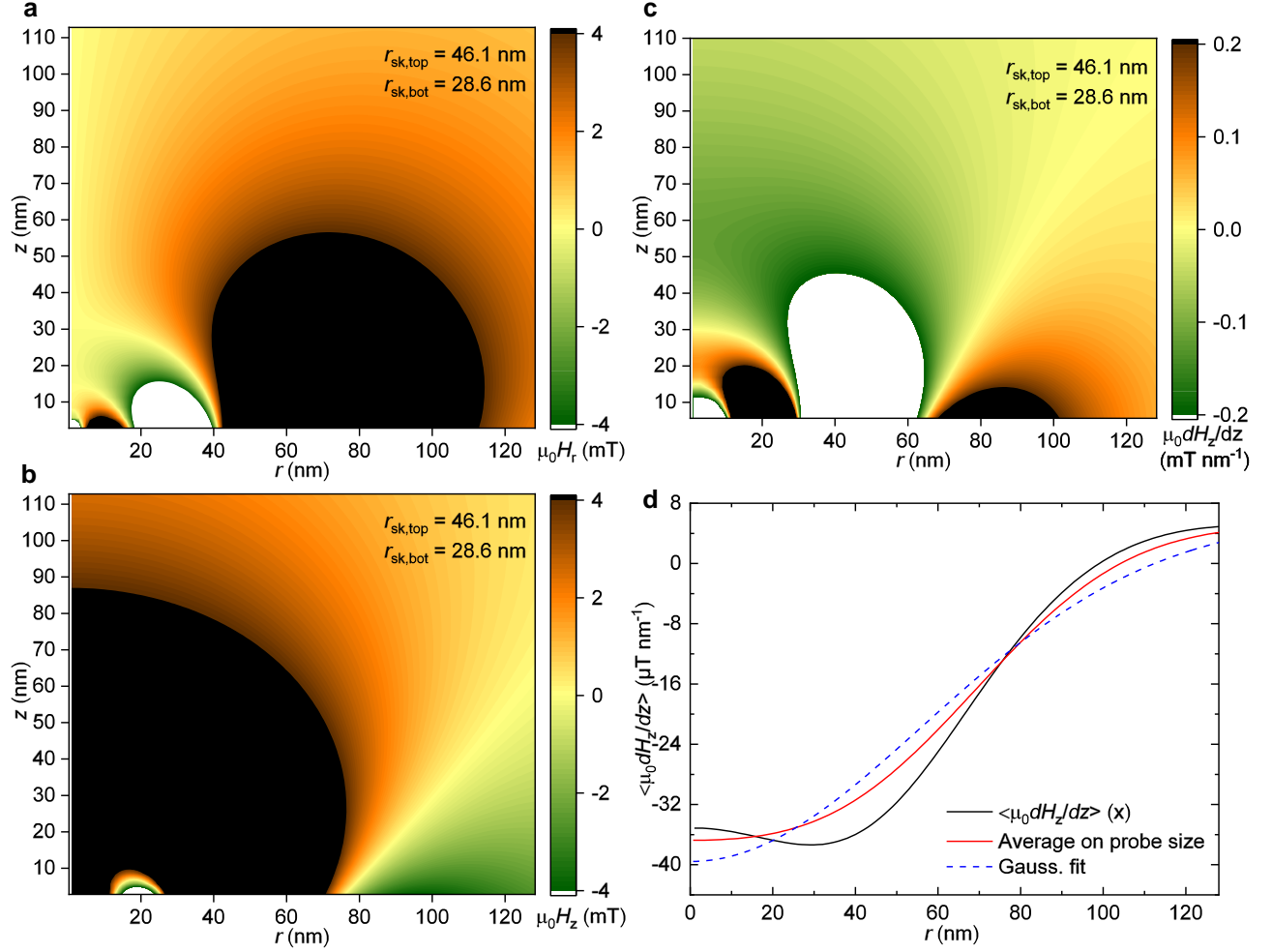


FIG. S22. Stray field generated by an antiferromagnetic skyrmion in the BL-SAF at $\mu_0 H_{\text{ext}} = 60 \text{ mT}$. **a–c.** Color maps of radial component (a), vertical component (b), and first partial z -derivative of the vertical component (c) of the stray field, encoded according to the colorscale given on the right. White (black) color corresponds to fields or field gradients larger (lower) than 4 mT or 0.20 mT nm^{-1} (-4 mT or -0.20 mT nm^{-1}). **d.** Field vertical gradient probed by the tip, averaged for tip oscillations (black line), and then averaged horizontally to take into account tip size of around 60 nm as a limit to the resolution (red line), and fit of this expected signal shape to a Gaussian peak function (dashed blue line).

Supplementary Note 9 – Model results for antiferromagnetic skyrmions in bottom and top layers

In Figs. S23a,b, we display the profiles of the antiferromagnetic skyrmions in the top layers of the SAF systems, together with the ones in the bottom layers for the varied values of D and $\mu_0 H_{\text{bias}}$ that we have studied in the main part of the article. They are very similar to the profiles in the bottom layers, only being slightly expanded, as this allows the system to reduce the dipolar energies and to get more DMI stabilizing energy, at the cost of some more RKKY energy. The fact that the profiles in the two layers are very similar to each other also appears in the perspective view of the antiferromagnetic skyrmion that we show in Fig. S23c.

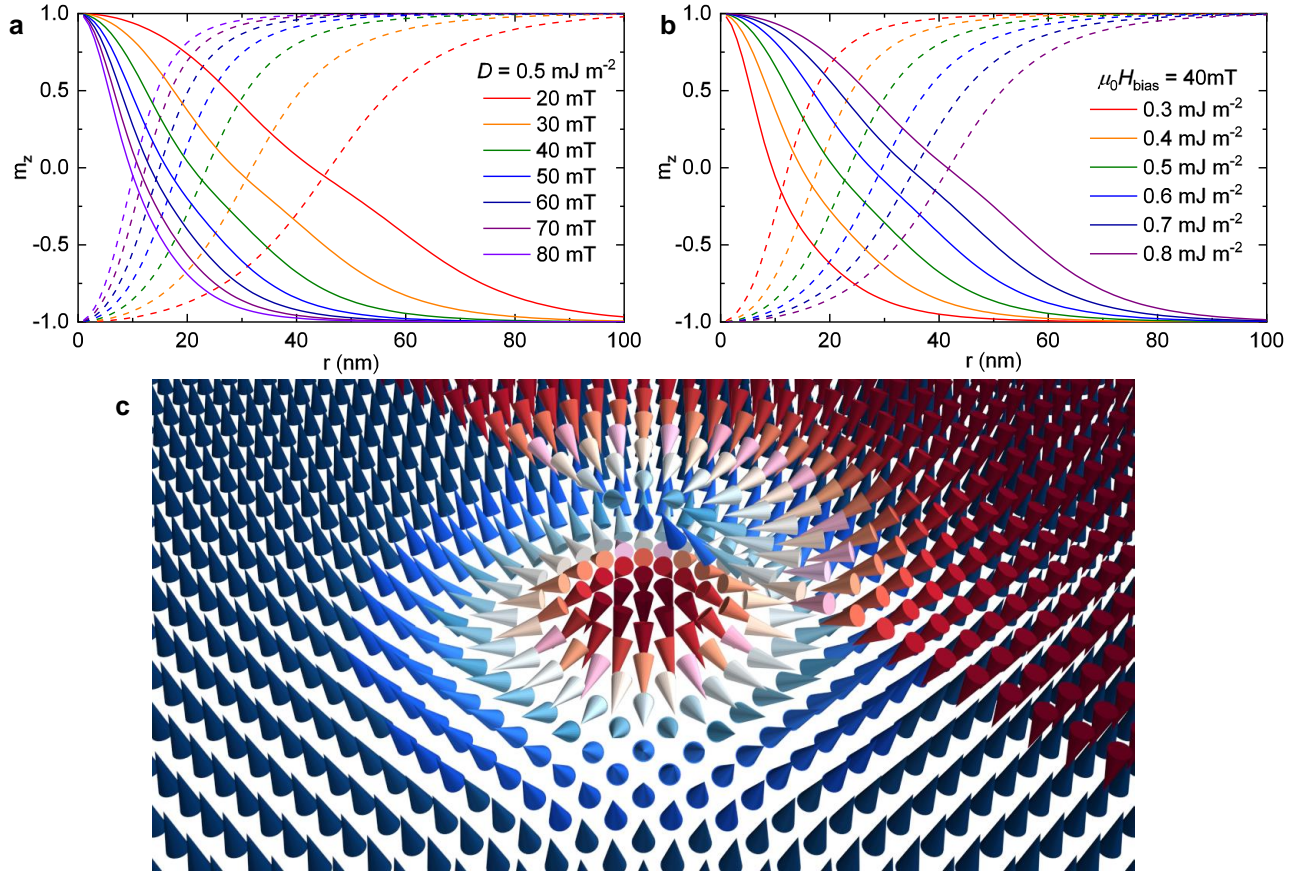


FIG. S23. Completed profiles of the antiferromagnetic skyrmions in the SAF system. **a,b.** Radial profiles of the vertical magnetization component m_z of the skyrmion for $\mu_0 H_{\text{bias}} = 20\text{--}80 \text{ mT}$ with $D = 0.5 \text{ mJ m}^{-2}$ (a), and for $D = 0.3\text{--}0.8 \text{ mJ m}^{-2}$ with $\mu_0 H_{\text{bias}} = 40 \text{ mT}$ (b). Top layer profiles are the plain lines, while bottom layer profiles are the dashed lines. **c.** A perspective view of the antiferromagnetic skyrmion in the SAF bilayer, where the top layer is cut at the center of the skyrmion.

Supplementary Note 10 – Influence of the dipolar fields on the antiferromagnetic skyrmions size and stability

In order to evaluate the influence of the interlayer dipolar fields on the antiferromagnetic skyrmion size and energy, we perform simulations similar to the ones described in the main part of the article, but replacing anisotropy energy E_{Ku} and dipolar fields energy E_{dip} by an effective anisotropy energy E_{Keff} . This is equivalent to consider a perfect compensation of the magnetic moments in the limit of zero layer spacing, keeping only intralayer dipolar interactions, but no interlayer interactions.

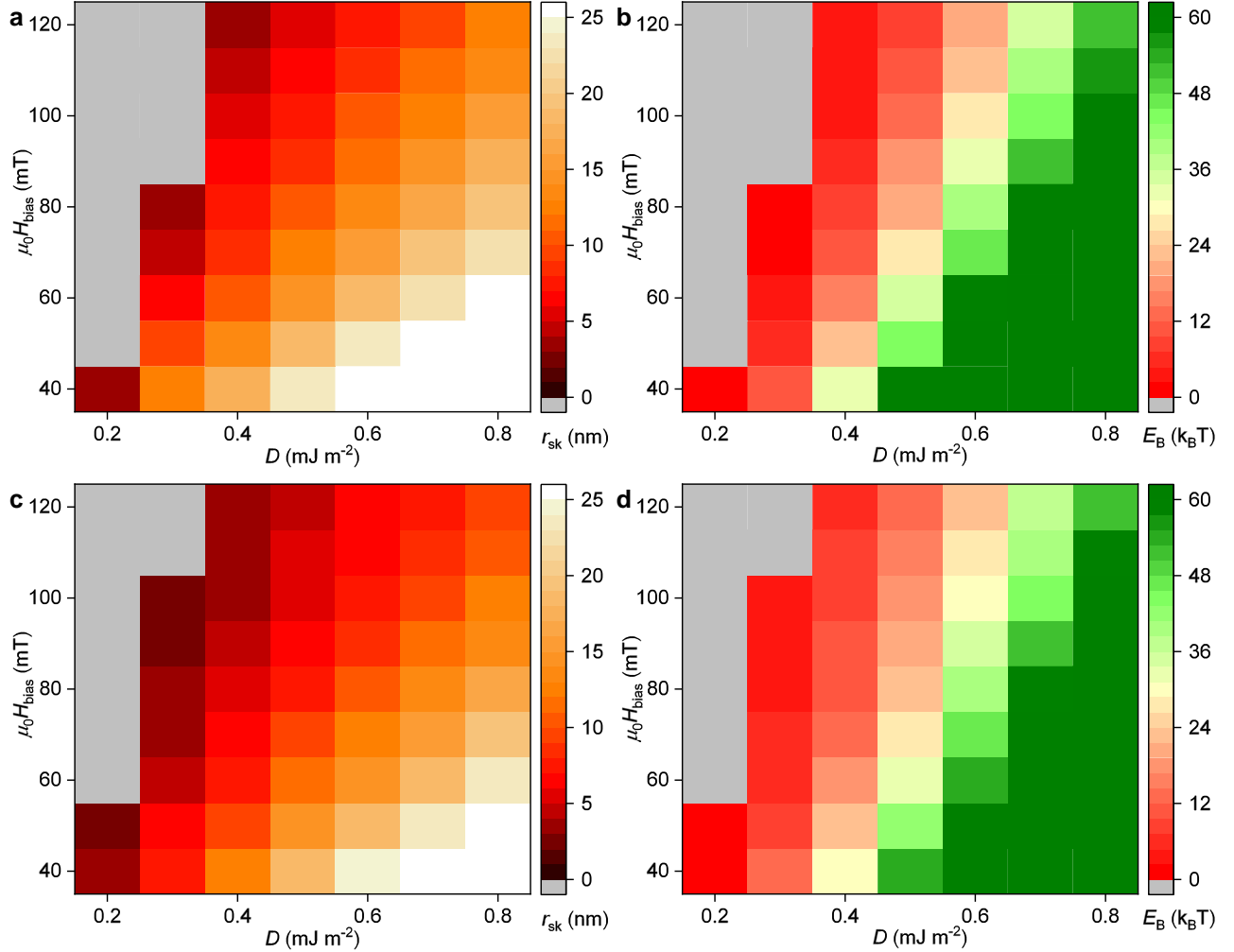


FIG. S24. Comparison of the two models, with and without long-range dipolar fields. **a–d.** Skyrmion radius r_{sk} (a,c) and energy barrier E_B (b,d) as a function of D and $\mu_0 H_{bias}$ with dipolar fields considered (a,c, reproducing panels from the main part of the article) and without long-range dipolar fields considered (b,d, using an effective anisotropy model). Values are given by the color scales on the right. Gray denotes collapsed skyrmions that show no energy barrier.

We compare results for the skyrmion radius r_{sk} and energy barrier E_B in Fig. S24. It appears that both models provide qualitatively similar results. However, neglecting the influence of long-range dipolar fields leads to a small overestimation of the dipolar energies. As a consequence, the stability conditions are slightly extended when neglecting long-range dipolar interactions, and the energy barriers are slightly inaccurate, while the skyrmion sizes are slightly underestimated.

We can conclude that a model neglecting long-range dipolar interactions is sufficient to provide the qualitative behavior of the biased SAF system, but is inaccurate for providing quantitative predictions for the antiferromagnetic skyrmion properties.

Supplementary Note 11 – Model results for antiferromagnetic skyrmions in SAF systems with 4 layers

By adding more antiferromagnetically coupled layers into the SAF system, we anticipate that the size and shape of the skyrmions remain almost identical, owing to the compensation of most of the dipolar fields. At the same time, the thermal stability is multiplied by a factor equal to the increase of magnetic volume of the skyrmion, due to rescaling of the skyrmion energies by this factor. In a SAF system with 4 layers, all energy barriers will be doubled compared to what we have presented with 2 layers, which is largely enough to stabilize stable room-temperature antiferromagnetic skyrmions below 10 nm in radius, as shown in Fig. S25.

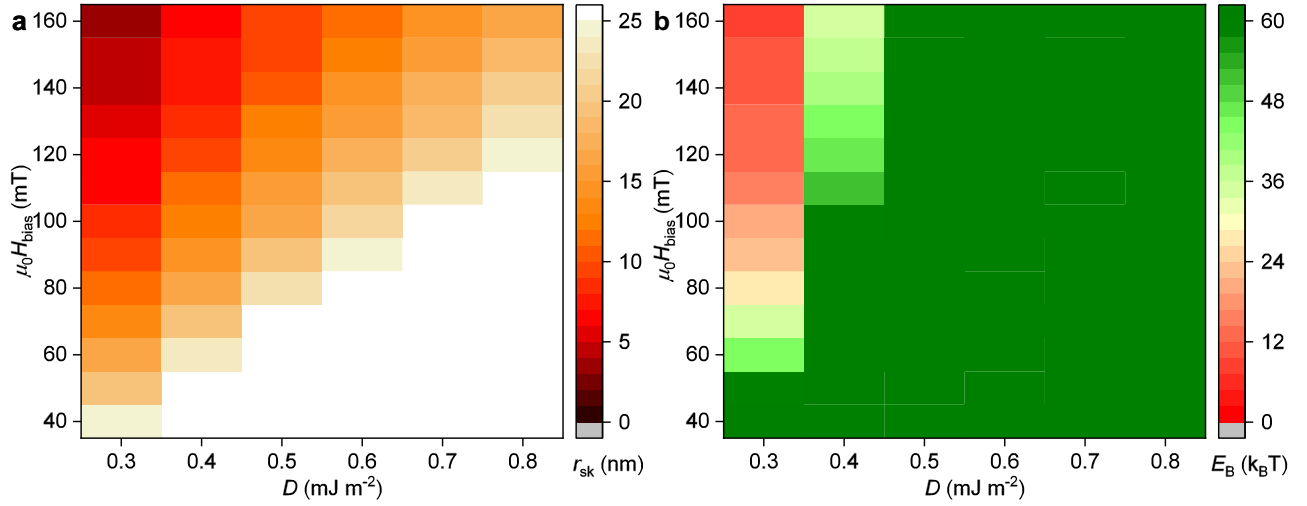


FIG. S25. Evaluation of sizes and energies of antiferromagnetic skyrmions in BL-SAF system where the SAF system is made of 4 magnetic layers. **a,b.** Skyrmion radius r_{sk} (a) and energy barrier E_B (b) as a function of D and $\mu_0 H_{bias}$, given by the color scales on the right.

Supplementary Note 12 – MFM observation of antiferromagnetic skyrmions at elevated temperatures

Because the stability of the magnetic skyrmions at elevated temperatures is crucial in view of current-induced motion experiments and related applications (which unavoidably generate heat in the system), we have verified this stability in temperature-dependent MFM measurements. We have imaged the antiferromagnetic skyrmions previously observed at room temperature in the BL-SAF system of the main part of the article, at higher temperatures, up to 150°C (Fig. S26). While the apparent size and associated contrast appear slightly different, the result is that these magnetic objects remain stable after significant heating. Note that the image at room temperature here (Fig. S26a) has a different level of contrast compared to the images of the main manuscript, due to the use of a different tip that was more suitable for temperature elevation.

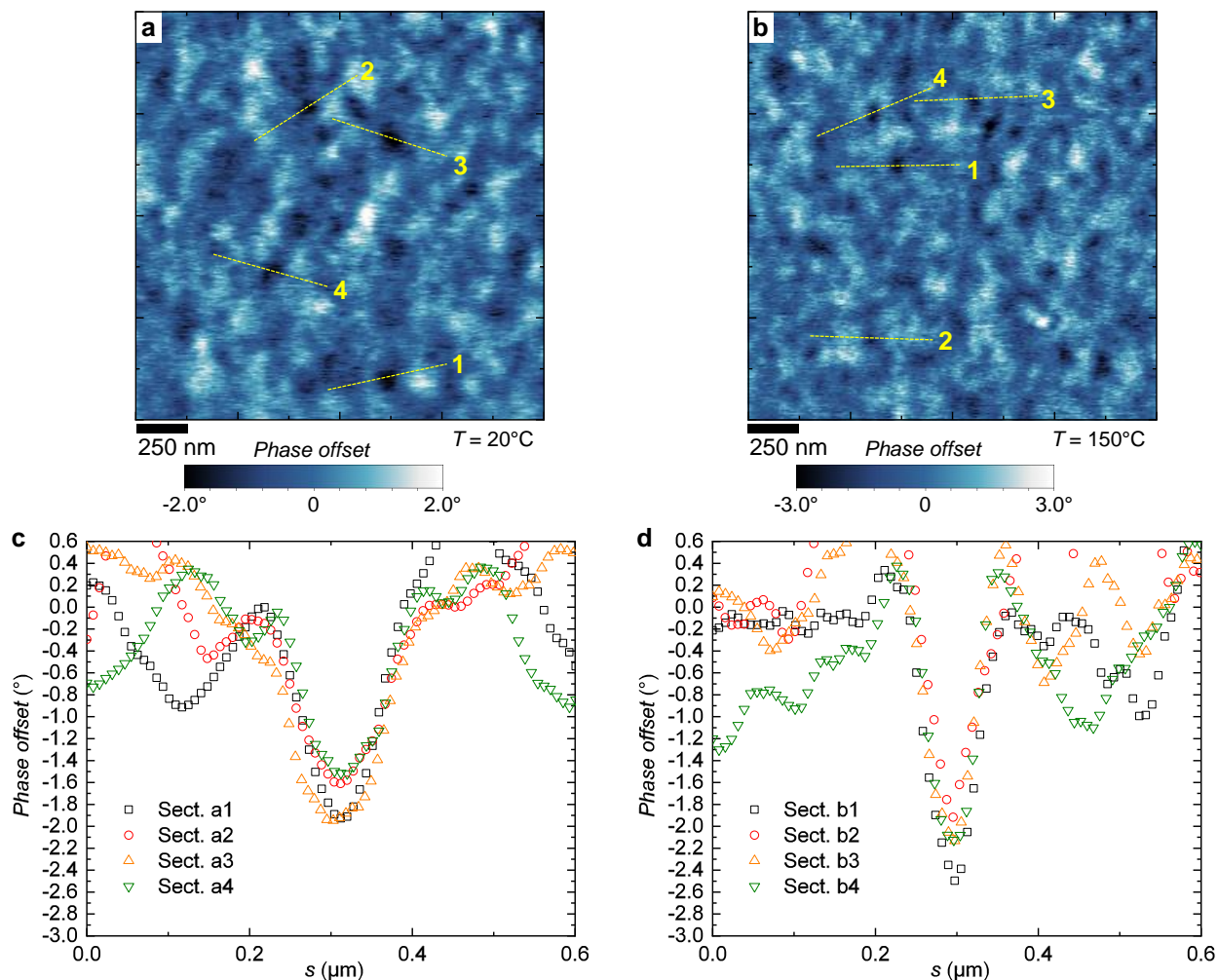


FIG. S26. **a,b.** MFM observations of the BL-SAF system under field $\mu_0 H_{\text{ext}} = 15$ mT, at $T = 20^\circ\text{C}$ (a) and at $T = 150^\circ\text{C}$ (b). **c.** Line sections a1, a2, a3 and a4 of the MFM signal (phase offset in lift mode) in the image for $T = 20^\circ\text{C}$. **d.** Line sections b1, b2, b3 and b4 of the MFM signal (phase offset in lift mode) in the image for $T = 150^\circ\text{C}$. The horizontal axis for line sections is the distance along each corresponding line in panels a and b.

Supplementary References

- [1] B. Dieny, J.-P. Gavigan, and J. Rebouillat, “Magnetisation processes, hysteresis and finite-size effects in model multilayer systems of cubic or uniaxial anisotropy with antiferromagnetic coupling between adjacent ferromagnetic layers,” *J. Phys.: Condens. Matter* **2**, 159–185 (1990).
- [2] G. Yu, A. Jenkins, X. Ma, S. A. Razavi, C. He, G. Yin, Q. Shao, Q. lin He, H. Wu, W. Li, W. Jiang, X. Han, X. Li, A. C. B. Jayich, P. K. Amiri, and K. L. Wang, “Room-temperature skyrmions in an antiferromagnet-based heterostructure,” *Nano Lett.* **18**, 980–986 (2018).
- [3] O. Hellwig, T. L. Kirk, J. B. Kortright, A. Berger, and E. E. Fullerton, “A new phase diagram for layered antiferromagnetic films,” *Nat. Mater.* **2**, 112–116 (2003).
- [4] S. Rohart and A. Thiaville, “Skyrmion confinement in ultrathin film nanostructures in the presence of dzyaloshinskii-moriya interaction,” *Phys. Rev. B* **88**, 184422 (2013).
- [5] M. Hervé, B. Dupé, R. Lopes, M. Bttcher, M. D. Martins, T. Balashov, L. Gerhard, J. Sinova, and W. Wulfhekel, “Stabilizing spin spirals and isolated skyrmions at low magnetic field exploiting vanishing magnetic anisotropy,” *Nat. Commun.* **9**, 1015 (2018).
- [6] C. Moreau-Luchaire, C. Moutafis, N. Reyren, J. Sampaio, C. A. F. Vaz, N. Van Horne, K. Bouzehouane, K. Garcia, C. Deranlot, P. Warnicke, P. Wohlhüter, J.-M. George, M. Weigand, J. Raabe, V. Cros, and A. Fert, “Additive interfacial chiral interaction in multilayers for stabilization of small individual skyrmions at room temperature,” *Nat. Nanotech.* **11**, 444–448 (2016).
- [7] S. Woo, K. Litzius, B. Krüger, M.-Y. Im, L. Caretta, K. Richter, M. Mann, A. Krone, R. M. Reeve, M. Weigand, P. Agrawal, I. Lemesch, M.-A. Mawass, P. Fischer, M. Kläui, and G. S. D. Beach, “Observation of room-temperature magnetic skyrmions and their current-driven dynamics in ultrathin metallic ferromagnets,” *Nat. Mater.* **15**, 501–506 (2016).
- [8] I. Lemesch, F. Büttner, and G. S. D. Beach, “Accurate model of the stripe domain phase of perpendicularly magnetized multilayers,” *Phys. Rev. B* **95**, 174423 (2017).
- [9] W. Legrand, J.-Y. Chauleau, D. Maccariello, N. Reyren, S. Collin, K. Bouzehouane, N. Jaouen, V. Cros, and A. Fert, “Hybrid chiral domain walls and skyrmions in magnetic multilayers,” *Sci. Adv.* **4**, eaat0415 (2018).
- [10] J. Lohau, S. Kirsch, A. Carl, G. Dumpich, and E. F. Wassermann, “Quantitative determination of effective dipole and monopole moments of magnetic force microscopy tips,” *J. Appl. Phys.* **86**, 3410–3417 (1999).
- [11] W. Legrand, N. Ronceray, N. Reyren, D. Maccariello, V. Cros, and A. Fert, “Modeling the Shape of Axisymmetric Skyrmions in Magnetic Multilayers,” *Phys. Rev. Appl.* **10**, 064042 (2018).